Remote sensing of ammonia point sources at high spatial resolution with satellite-based imaging spectrometers

Javier Roger[1,2*], Adriana Valverde[1], Javier Gorroño[1], Zhipeng Pei[3], Itziar Irakulis-Loitxate[1,4], Luis Guanter[1,5]

[1] *Research Institute of Water and Environmental Engineering (IIAMA), Universitat Politècnica de València (UPV), Valencia, Spain.*
[2] *Now at: Institute of Environmental Physics (IUP), University of Bremen, Bremen, Germany.*
[3] *School of Remote Sensing and Information Engineering, Wuhan University, Wuhan, China.*
[4] *International Methane Emissions Observatory, United Nations Environment Programme.*
[5] *Environmental Defense Fund, Amsterdam, the Netherlands.*

[*] To whom correspondence should be addressed; E-mail: jroger@iup.physik.uni-bremen.de

Ammonia (NH_3) emissions play a key role in air pollution and the disruption of the nitrogen cycle. Global emissions of ammonia are expected to increase in the future, making their monitoring essential to better understand their impacts and to support effective environmental policies. Recent studies have demonstrated the potential of satellite imaging spectrometers operating in the shortwave infrared (SWIR) to identify ammonia point source emissions, mostly from fertilizer plants. In this work, we extend these observations to the current fleet of SWIR imaging spectrometers, including EMIT, EnMAP, PRISMA, GF-5A AHSI, and MethaneSat and provide a first systematic assessment of ammonia plume detection and quantification capabilities. We derive instrument-specific detection limits as a function of retrieval noise and wind speed, and obtain plume quantification models following the IME method, also accounting for a range of potential ammonia atmospheric lifetime values (1 h to 48 h). Under favorable conditions, we find detection thresholds of approximately 0.5 t/h and 0.8 t/h for EnMAP and EMIT, respectively. Using this framework, we present multiple ammonia plume detections from fertilizer plants and provide consistent emission estimates across different sensors. Finally, a 2.5-year time series over a fertilizer plant in Iraq demonstrates the potential of the current SWIR imaging spectrometer constellation to monitor ammonia point sources.

Introduction

Ammonia (NH_3) emissions trigger air pollution through the formation of particulate matter with a diameter of 2.5 μm or smaller ($PM_{2.5}$)[1]. Fine particulate pollution poses a major threat to human health and is considered among the leading environmental risk factors contributing to global mortality[2]. Worldwide, exposure to elevated $PM_{2.5}$ levels has been

linked to approximately three million premature deaths annually[3]. Ammonia emissions also disrupt the nitrogen cycle, causing severe consequences such as soil acidification or biodiversity loss[4]. This disruption contributes to global warming through the formation of nitrous oxide (N_2O), a greenhouse gas with a global warming potential around 273 times stronger than carbon dioxide (CO_2) over a 100-year period[5]. In addition, ammonia production results in around 1% of total CO_2 emissions around the world, since it strongly depends on fossil fuels[6]. Since pre-industrial times, anthropogenic activities have increased global ammonia emissions by a factor of 2–5[7], and emissions are expected to continue rising in the coming years if no mitigation measures are implemented[8,9]. Therefore, monitoring ammonia emissions is essential to better understand their impacts and support effective environmental policies.

Around 80% of global ammonia emissions are originated from agriculture, including livestock and fertilizer related activities[10]. Losses from livestock waste management and volatilization from fertilizer application account for an important fraction of these emissions[11]. Other important emission sources are fertilizer production plants, which rely on ammonia produced via the Haber–Bosch process and are among the strongest anthropogenic point sources[12]. These localized emissions remain poorly constrained, and satellite observations from IASI[13] have shown that they are often substantially underestimated in bottom-up emission inventories[14]. IASI and other similar satellite sounders, such as CrIS[15] and AIRS[16], exploit the ammonia absorption features in the thermal infrared (TIR). At this spectral range, an accurate knowledge of thermal contrast is required, which is a general limitation of thermal infrared measurements[12]. In addition, the coarse spatial resolution of these instruments (> 12 km) limits their ability to resolve individual point sources, which challenges the emission attribution to an specific source. On the other hand, airborne TIR instruments such as HyTES[17] and Mako[18] have demonstrated successful attribution of ammonia point sources. However, continuous monitoring through airborne campaigns is expensive and inefficient.

Ammonia also exhibits non-negligible absorption features in the shortwave infrared (SWIR), where current satellite instruments are sensitive. In Figure 1, we show the ammonia transmittance spectrum (red) along with those of water vapor (H_2O, blue), methane (CH_4, orange), CO_2 (green), and N_2O (purple) in the 1400 nm to 2500 nm spectral range. Several ammonia absorption windows are found within this range: the 1500 nm window (A), 1650 nm window (B), 2000 nm window (C), and 2300 nm window (D). The presence of these well-defined SWIR absorption features opens the possibility of retrieving ammonia signals directly in reflected solar radiation, rather than relying on thermal emission measurements. Consequently, ammonia characterization in the SWIR avoids the need to account for thermal contrast effects, which complicate TIR-based measurements. Satellite high-resolution imaging spectrometers operating in the SWIR have already demonstrated their ability to characterize emissions of gases such as methane[19] and CO_2[20]. This experience provides a strong foundation for extending similar methodologies to am-

monia.

[Figure 1 about here.]

Balasus et al.[21] reported three ammonia plumes from fertilizer plants using Tanager-1 observations, demonstrating the potential of high-resolution SWIR imaging spectroscopy for ammonia plume characterization. Tanager-1[22] combines a spatial resolution of 30 m with a spectral sampling and resolution of approximately 5 nm. In addition, Ruzicka et al.[23] applied an automated plume detection framework to a large portion of the EMIT[24] data archive and identified ammonia plumes from multiple source types. In the SWIR, EMIT provides a spectral sampling and resolution of around 7.5 nm and 9 nm, respectively, at a spatial resolution of 60 m.

Beyond these missions, several existing imaging spectrometers possess characteristics that make them promising candidates for ammonia plume detection. These include EnMAP[25], PRISMA[26], and GF-5A AHSI[27], which all offer spatial resolutions of about 30 m and spectral sampling and resolution relatively close to that of EMIT. We also consider MethaneSAT[28], whose very fine spectral sampling and resolution in the 1650 nm absorption window (0.08 nm and 0.25 nm, respectively) may compensate, at least partially, for its coarse spatial resolution ($\sim$100 m $\times$ 400 m). A multisatellite constellation of SWIR imaging spectrometers could therefore enable frequent monitoring of ammonia point sources, complementing the ow spatial resolution provided by TIR instruments. Moreover, the extensive heritage developed for methane and CO_2 is expected to accelerate progress in the ammonia characterization using this kind of instruments, as many of the retrieval and plume quantification techniques developed for these gases can be adapted to ammonia observations.

In this work, we assess the potential of several satellite high-resolution imaging spectrometers operating in the SWIR for the detection and quantification of ammonia point source emissions. We perform a sensitivity analysis to determine ammonia plume detection limits for the EMIT and EnMAP missions, with results that can be largely generalized to PRISMA, GF-5A AHSI, and Tanager-1. In addition, instrument-specific plume quantification models are obtained, also considering the relatively short lifetime of ammonia. These are empirical models that establish the relationship between the emission rate and the wind speed at measurement time. Next, we showcase ammonia plumes detected with EnMAP, PRISMA, GF-5A AHSI, MethaneSAT, and EMIT observations along with their related emission rates. Finally, we demonstrate the capability of the current fleet of imaging spectrometers to jointly monitor and quantify ammonia point source emissions over time through a 2.5-year analysis of a fertilizer plant in Iraq.

Methods and Materials

Ammonia emissions were identified through the visual inspection of concentration-path length enhancement maps (α), defined in units of parts-per-million meter (ppm·m). These were obtained with the matched filter method as in Thompson et al.[29]. We additionally carried out radiance filtering based on supervised thresholding and applied an additional matched filter iteration to exclude potential plume pixel candidates from the method input statistics[30]. For a range of gas enhancements and geometrical air mass factors, Lookup tables (LUTs) of high-resolution radiance spectra (0.1 nm) were generated. These were used to extract the unit gas absorption spectrum, which is needed to run the matched filter method (Section S1). We built LUTs for ammonia, but also for methane, carbon dioxide, and water vapor, since we also use them to analyze whether ammonia plumes were correlated with other gases. These LUTs are open to the public and can be used to reproduce this work (Data and Code Availability).

For EnMAP, EMIT, PRISMA, and GF-5A AHSI we exploited the 2300 nm, 1500 nm, and 2000 nm windows, while for MethaneSAT we exploited the 1650 nm window due to different spectral coverage (Figure 1). Even though some emissions were detected with MethaneSAT, it is unclear whether the matched filter retrieval values are low-biased[31]. To avoid any quantitative misinterpretation from MethaneSAT data, we label ammonia retrieval units as arbitrary units (A.U.). We therefore decide to exclude this mission from the main analysis and focus on the remaining ones, which share more similar instruments.

We carried out a sensitivity analysis to determine the plume detection limit (Q_{det}) in the different retrieval windows (Section S2). We defined Q_{det} as the emission rate at which we can approximately detect half of the plumes. For this purpose, we adapted the WRF-LES simulation dataset accessible in[32] and described in Gorroño et al.,[33] to the ammonia molar mass. Then, we added random noise extracted from ammonia retrievals to obtain realistic maps, similar to those we would obtain with the matched filter method. Next, we applied an iterative methodology similar to Roger et al.[30] until we obtain the emission rate at which the plume could be detected. All the results were combined to deduce a relationship among the detection limit, the retrieval noise, and wind speed. We also accounted for the relatively short lifetime (τ) of ammonia, and considered $\tau = 1$ h, $\tau = 12$ h, and $\tau = 48$ h[14], according to the variability shown in the existing literature. We also considered $\tau \to \infty$, as for those gases with longer lifetimes such as methane and carbon dioxide. Since $\tau = 12$ h and $\tau = 48$ h provided similar results to $\tau = \infty$, we only kept the results for $\tau = 1$ h and $\tau \to \infty$ as representative cases. Intermediate τ values yield results that lie between these two cases and exhibit a smooth transition approximately consistent with a logarithmic dependence on τ.

Global ammonia source catalogues derived from IASI measurements[14,34] were used

to search emissions throughout the EMIT, EnMAP, PRISMA, GF-5A AHSI, and MethaneSAT archives. Particular attention was given to sources classified as "fertilizer industry", as these are typically associated with the strongest ammonia point sources[12]. Our instruments are better suited to detecting concentrated point-source emissions than the more diffuse emissions characteristic of agricultural activities. For those scenes with potential emission, we obtained the retrievals from all the available bands. Except for the MethaneSAT case where we only explore the 1650 nm window, we select the 2300 nm window as the main band for detection due to the retrieval's higher SNR. If the plume was found in the other retrieval bands, it supported the detection. Moreover, we also checked whether there was correlation with other gases, i.e. CH_4, CO_2, and H_2O, to identify potential false positives. All the emission detections along with other acquisition details are listed in Table S1.

Ammonia plume quantification was carried out following the IME method[35,36]. The wind speed needed for the quantification was extracted from the GEOS-FP product[37]. We again used WRF-LES simulations to obtain plume quantification models as Gorroño et al.[33] (Section S3). We accounted for $\tau = 1$ h and $\tau \to \infty$, and for the EMIT, EnMAP, GF-5A AHSI, and PRISMA instruments. Details about instrument-specific models for plume quantification can be found in Table S3. Note that the code that is used to obtain the α maps together with the quantification is also open to the public (Data and Code Availability).

We also evaluated the time-series of the emissions of a fertilizer plant in Iraq during the time spanning between September 2023 to March 2026. Fertilizer production facilities are typically running with no interruptions[38], resulting in ammonia emissions from several stages of the process, including neutralizers, evaporators, and coolers, as well as fugitive losses from storage and associated equipment[39]. As in Noppen et al.,[12], we assume that the source is continuously emitting, as emissions were detected in most acquisitions covering this source. Emission rate values from those plumes that passed our quality screening were added to the time-series. Quality screening was mainly based on a supervised assessment to determine whether the plume was cut by surrounding artifacts and whether it could be clearly distinguished from the industrial facilities. Then, we attempt to extract the mean daily emission rate in the time period where we have detections based on similar approach to that of Guanter et al.[40]. For this purpose, we combine second-order polynomial fits with multivariate Monte Carlo simulations. The samples assume a 50% error correlation, while uncertainties are reported as two standard deviations to account for the large scatter and scarcity of data points (Section S7).

Results and Discussion

Figure 2 is the result of our ammonia plume detection limit assessment. We can observe the relationship among the wind speed at 10 m above surface (U_{10}), the retrieval noise (σ_{ret}), and the plume detection limit (Q_{det}), which was defined as the emission rate at which we can detect approximately half of the plumes. Red lines depict those $\{\sigma_{\mathrm{ret}}, U_{10}\}$ combinations that are equivalent to a given Q_{det} value. This relationship is showed for the EnMAP (left panel) and EMIT (right panel) instruments. The relationship derived for EnMAP can also be applied to GF-5A AHSI and PRISMA data, as these instruments share the same pixel size (30 m) and their retrieval noise levels are expected to fall within the range considered in our analysis. Although Tanager-1 exhibits the same pixel size, it is likely to achieve lower retrieval noise, which may place it outside the retrieval noise range explored here. In contrast, the results for the EMIT mission are shown separately, as it is the only instrument with a pixel size of 60 m. EnMAP and EMIT retrievals based on the 2300 nm, 1500 nm, and 2000 nm windows were used to define the range of σ_{ret} values. This was done to understand why plumes are detectable in some spectral windows but not in others. Note that the definition of plume detectability is set similarly to Roger et al.,[30] (Section S2). We also found that EMIT requires higher precision to detect a plume with a given emission rate, although its performance is generally sufficient to satisfy this requirement due to its coarser pixel size. Altogether, these plots provide a framework for assessing ammonia plume detectability under varying retrieval noise and wind conditions.

[Figure 2 about here.]

Based on the previous results, ammonia plume detection and quantification was mainly based on the 2300 nm window. The higher SNR in the α maps makes the plume pixels less contaminated by noise in comparison to the retrievals from the 1500 nm and 2000 nm windows. However, there appear to be some advantages to using a wider spectral window (1400 nm–2500 nm) for detection as in Roger et al.[41] with methane. While our tests showed areas with new artifacts and noisier areas in comparison to the plume signal, there were other areas with artifact attenuation and lower noise that benefited plume detectability (Section S6). Ruzicka et al.[23] developed an automatic methane plume detection model that was applied to EMIT data and found that better performance was obtained using a wide spectral window instead of just using the main absorption window. This model was also applied to ammonia, but plume detections were obtained by combining the individual retrievals coming from the 3 different absorption windows. Similarly to methane, our results indicate that the use of a wide window might improve the performance of this automatic plume detection model for ammonia.

Some examples of ammonia plumes obtained with EMIT, MethaneSAT, GF-5A AHSI, EnMAP, and PRISMA are shown in Figure 3. Masked plumes are overlaid on high-

resolution Google Earth RGB images. Map scale, acquisition date, country, plume source location coordinates, and emission rate values considering τ = ∞ and τ = 1 h are also shown. All these sources were related to the fertilizer industry, which is considered the most suitable sector for detection due to its strong and localized emissions. To further support these detections, we investigated the plumes shown in this figure using multiple ammonia absorption windows (Section S4) and through correlation analyses with other gases (Section S5), where non-masked retrievals are shown.

[Figure 3 about here.]

The EnMAP acquisition over the Uzbekistan source was taken only three days after Tanager-1 detected the same source[21]. While we obtain a Q($\tau = \infty$) = 0.59 $\pm$ 0.18 t/h and Q($\tau = 1$ h) = 0.62 $\pm$ 0.18 t/h for EnMAP, a Q($\tau = \infty$) = 0.74 $\pm$ 0.21 t/h was found for the Tanager-1 detection, which shows consistency. Apart from the emissions shown in Figure 3, other plumes from these and other sources were detected and quantified when possible (Table S1). We checked that the automated plume detection model from Ruzicka et al.[23] applied to the EMIT catalogue could detect plumes from all the sources shown in Figure 3 and additional ones. Out of this list, we detected ammonia plumes originating from fertilizer industry facilities in Iran and Borneo with EMIT data. These non-detections from the Ruzicka et al.[23] model might be due to a relatively conservative thresholding to avoid false positives.

Exploiting other mission data catalogues such as done for EMIT in Ruzicka et al.[23] would be beneficial for plume detection, since it would facilitate the joint monitoring potential of the current satellite fleet of imaging spectrometers. To demonstrate this potential, Figure 4 presents the case of a fertilizer plant in Iraq, where multiple plume detections were obtained using data from several missions. The multisatellite monitoring was used to quantify the total amount of emitted ammonia during the time spanning between September 2023 to March 2026. We acknowledge that even assuming two standard deviations for the time series uncertainty, we find a mismatch with the instrument measurements due to the large scatter and scarcity of data points. More measurements would be needed to obtain a more robust estimate, but this result already provides interesting information about this specific source. Our fittings suggest a decreasing trend in emitted ammonia through time. We also observe a difference of 3 % between the mean emission rate obtained considering $\tau \rightarrow \infty$ and $\tau = 1$ h, which is negligible when considering the large error bars. The mean emission rate of this source is 5.6 t/h, which is comparable to the amount of methane released by massive super-emitters[42]. In addition to contributing to human mortality as one of the main precursors of secondary particulate matter formation, this excess of ammonia also leads to disruptions of the nitrogen cycle, such as the acidification of water bodies and precipitation. In this regard, this source exhibits an acidification potential approximately equivalent to 94 kt of SO_2[43] during the analyzed time range. Each

tonne of ammonia produced also implies the generation of 2.4 t of CO_2[44]. The amount of ammonia emitted is equivalent to 120 kt CO_2, but this value is expected to be significantly higher when accounting for the total ammonia production related to this source. If known, it would be possible to estimate the ammonia leakage rate related to the source, which may be useful for assessing potential emission mitigation strategies.

[Figure 4 about here.]

The mean emission rate for this source is approximately 10 times larger than that reported by Van Damme et al.[14], which was obtained from a 9-year average spanning 2008 to 2016. However, our time series covers the period from September 2023 to March 2026 ($\sim$2.5 years). It is therefore possible that changes in the fertilizer plant production may have occurred during this period. While IASI sampled the source twice per day (morning and night), the temporal sampling of our instruments is generally limited to either the morning or afternoon. Potential emission variability throughout the whole day may be overlooked. In addition, our estimate was based only on emissions that produced a detectable plume, which are also associated with higher emission rates. Lower emissions that resulted only in enhancements over the facility were discarded because they could not be quantified. Therefore, there is a clear bias toward higher emission estimates, which may influence our final results. In the future, a more intensive sampling from instruments with lower detection limits such as Tanager-1 could contribute to more accurate estimates. Because ammonia point sources are underestimated in bottom-up inventories and cannot be adequately resolved with coarse spatial resolution instruments such as IASI, high-resolution satellite imaging spectrometers can be used to fill this gap.

There is a list of current and upcoming SWIR instruments that may also be suitable for ammonia plume detection. Here we highlight a selection of potential missions. Among current instruments, we consider the airborne AVIRIS family and WorldView-3. The AVIRIS family[45] shares similar characteristics to most of the satellite-based instruments analyzed in this work. WorldView-3[46], with its very high spatial resolution (3.7 m) and four multispectral bands covering the 2300 nm window, may also enable feasible detections. Among upcoming missions, we consider the Carbon Mapper constellation, CHIME, and Sentinel-2 NG. The Carbon Mapper constellation[22] will expand the number of instruments with specifications similar to Tanager-1. CHIME[47] is expected to achieve a similar performance to that of EnMAP and PRISMA, while benefiting from improved temporal sampling. Similarly to WorldView-3, Sentinel-2 NG may exploit multiple bands covering the 2300 nm window[48], which could enhance global-scale monitoring of ammonia point sources. Overall, these and other missions measuring in the SWIR spectrum might expand the fleet of instruments available for monitoring ammonia emissions.

Data and Code Availability

- Code to run the retrievals, plume delineation, and quantification can be found in https://github.com/jarojuan96/HS_tool. The default atmosphere file and the LUTs used for this work can also be found in this repository.
- L1 data from EnMAP, PRISMA, EMIT, and MethaneSAT are open to the public and can be found in their corresponding data portals. GF-5A AHSI data was obtained through personal communication with Chinese institutions.

References

1. Malm, W. C., Schichtel, B. A., Pitchford, M. L., Ashbaugh, L. L. & Eldred, R. A. Spatial and monthly trends in speciated fine particle concentration in the united states. *Journal of Geophysical Research: Atmospheres* **109** (2004). URL https://agupubs.onlinelibrary.wiley.com/doi/abs/10.1029/2003JD003739. https://agupubs.onlinelibrary.wiley.com/doi/pdf/10.1029/2003JD003739.

2. Lim, S. S. *et al.* A comparative risk assessment of burden of disease and injury attributable to 67 risk factors and risk factor clusters in 21 regions, 1990–2010: a systematic analysis for the global burden of disease study 2010. *The Lancet* **380**, 2224–2260 (2012). URL https://www.sciencedirect.com/science/article/pii/S0140673612617668.

3. Cohen, A. J. *et al.* Estimates and 25-year trends of the global burden of disease attributable to ambient air pollution: an analysis of data from the global burden of diseases study 2015. *The Lancet* **389**, 1907–1918 (2017). URL https://www.sciencedirect.com/science/article/pii/S0140673617305056.

4. Erisman, J. W. *et al.* Consequences of human modification of the global nitrogen cycle. *Philosophical Transactions of the Royal Society B: Biological Sciences* **368**, 20130116 (2013). URL https://doi.org/10.1098/rstb.2013.0116.

5. Weber, J., Keeble, J., Abraham, N. L., Beerling, D. J. & Martin, M. V. Global agricultural n2o emission reduction strategies deliver climate benefits with minimal impact on stratospheric o3 recovery. *npj Climate and Atmospheric Science* **7**, 121 (2024). URL https://doi.org/10.1038/s41612-024-00678-2.

6. Erisman, J. W. Ammonia for food and fuels in a sustainable future. *One Earth* **9**, 101621 (2026). URL https://www.sciencedirect.com/science/article/pii/S2590332226000229.

7. Lamarque, J.-F. *et al.* Global and regional evolution of short-lived radiatively-active gases and aerosols in the representative concentration pathways. *Climatic Change* **109**, 191– (2011). URL https://doi.org/10.1007/s10584-011-0155-0.

8. Moss, R. H. *et al.* The next generation of scenarios for climate change research and assessment. *Nature* **463**, 747–756 (2010). URL https://doi.org/10.1038/nature08823.

9. International Energy Agency. Ammonia technology roadmap. Tech. Rep., International Energy Agency (2021). URL https://www.iea.org/reports/ammonia-technology-roadmap. CC BY-NC 3.0 IGO.

10. Zhu, L. *et al.* Sources and impacts of atmospheric nh3: Current understanding and frontiers for modeling, measurements, and remote sensing in north america. *Current Pollution Reports* **1**, 95–116 (2015). URL https://doi.org/10.1007/s40726-015-0010-4.

11. Erisman, J. W. *et al.* Nitrogen: Too much of a vital resource. Tech. Rep., WWF Netherlands, Zeist, The Netherlands (2015). URL http://www.louisbolk.org/downloads/3005.pdf. Science Brief.

12. Noppen, L. *et al.* Constraining industrial ammonia emissions using hyperspectral infrared imaging. *Remote Sensing of Environment* **291**, 113559 (2023). URL https://www.sciencedirect.com/science/article/pii/S0034425723001104.

13. Clerbaux, C. *et al.* The iasi/metop1 mission: First observations and highlights of its potential contribution to gmes2. *Space Research Today* **168**, 19–24 (2007). URL https://www.sciencedirect.com/science/article/pii/S0045873207800465.

14. Van Damme, M. *et al.* Industrial and agricultural ammonia point sources exposed. *Nature* **564**, 99–103 (2018). URL https://doi.org/10.1038/s41586-018-0747-1.

15. Shephard, M. W. & Cady-Pereira, K. E. Cross-track infrared sounder (cris) satellite observations of tropospheric ammonia. *Atmospheric Measurement Techniques* **8**, 1323–1336 (2015). URL https://amt.copernicus.org/articles/8/1323/2015/.

16. Warner, J. X., Wei, Z., Strow, L. L., Dickerson, R. R. & Nowak, J. B. The global tropospheric ammonia distribution as seen in the 13-year airs measurement record. *Atmospheric Chemistry and Physics* **16**, 5467–5479 (2016). URL https://acp.copernicus.org/articles/16/5467/2016/.

17. Kuai, L. *et al.* Quantification of ammonia emissions with high spatial resolution thermal infrared observations from the hyperspectral thermal emission spectrometer (hytes) airborne instrument. *IEEE Journal of Selected Topics in Applied Earth Observations and Remote Sensing* **12**, 4798–4812 (2019).

18. Hasheminassab, S. *et al.* Tracing ammonia emission sources in california's salton sea region: insights from airborne longwave-infrared hyperspectral imaging and ground monitoring. *Atmospheric Chemistry and Physics* **25**, 11935–11950 (2025). URL https://acp.copernicus.org/articles/25/11935/2025/.

19. Jacob, D. J. *et al.* Quantifying methane emissions from the global scale down to point sources using satellite observations of atmospheric methane. *Atmospheric Chemistry and Physics* **22**, 9617–9646 (2022). URL https://acp.copernicus.org/articles/22/9617/2022/.

20. Cusworth, D. H. *et al.* Quantifying global power plant carbon dioxide emissions with imaging spectroscopy. *AGU Advances* **2**, e2020AV000350 (2021). URL https://agupubs.onlinelibrary.wiley.com/doi/abs/10.1029/2020AV000350. E2020AV000350 2020AV000350, https://agupubs.onlinelibrary.wiley.com/doi/pdf/10.1029/2020AV000350.

21. Balasus, N. *et al.* Mapping ammonia emission plumes using shortwave infrared imaging spectroscopy. *Proceedings of the National Academy of Sciences* **123**, e2605694123 (2026). URL https://www.pnas.org/doi/abs/10.1073/pnas.2605694123. https://www.pnas.org/doi/pdf/10.1073/pnas.2605694123.

22. Duren, R. *et al.* The carbon mapper emissions monitoring system. *Atmospheric Measurement Techniques* **18**, 6933–6958 (2025). URL https://amt.copernicus.org/articles/18/6933/2025/.

23. Růžička, V. *et al.* Fully automatic trace gas plume detection (2026). URL https://arxiv.org/abs/2605.03372. 2605.03372.

24. Connelly, D. S. *et al.* The emit mission information yield for mineral dust radiative forcing. *Remote Sensing of Environment* **258**, 112380 (2021). URL https://www.sciencedirect.com/science/article/pii/S0034425721000985.

25. Guanter, L. *et al.* The enmap spaceborne imaging spectroscopy mission for earth observation. *Remote Sensing* **7**, 8830–8857 (2015). URL https://www.mdpi.com/2072-4292/7/7/8830.

26. Loizzo, R. *et al.* Prisma: The italian hyperspectral mission. In *IGARSS 2018 - 2018 IEEE International Geoscience and Remote Sensing Symposium*, 175–178 (2018).

27. Liu, Y.-N. *et al.* The advanced hyperspectral imager: Aboard china's gaofen-5 satellite. *IEEE Geoscience and Remote Sensing Magazine* **7**, 23–32 (2019).

28. Environmental Defense Fund. Methanesat (2021). URL https://www.methanesat.org/. Accessed: 12 June 2026.

29. Thompson, D. R. *et al.* Space-based remote imaging spectroscopy of the aliso canyon ch4 superemitter. *Geophysical Research Letters* **43**, 6571–6578 (2016). URL https://agupubs.onlinelibrary.wiley.com/doi/abs/10.1002/2016GL069079. https://agupubs.onlinelibrary.wiley.com/doi/pdf/10.1002/2016GL069079.

30. Roger, J., Guanter, L. & Gorroño, J. Assessing the detection of methane plumes in offshore areas using high-resolution imaging spectrometers. *Atmospheric Measurement Techniques* **18**, 5545–5567 (2025). URL https://amt.copernicus.org/articles/18/5545/2025/.

31. Guanter, L. *et al.* Surveying methane point-source super-emissions across oil and gas basins with methanesat. *Atmospheric Chemistry and Physics* **26**, 2941–2963 (2026). URL https://acp.copernicus.org/articles/26/2941/2026/.

32. Gorroño, J., Pei, Z. & Guanter, L. Benchmark simulations for methane emissions validation and sensitivity studies (2026). URL https://doi.org/10.5281/zenodo.18161182.

33. Gorroño, J., Pei, Z., Valverde, A. & Guanter, L. Considering the observation and illumination angular configuration for an improved detection and quantification of methane emissions. *Atmospheric Measurement Techniques* **19**, 1245–1257 (2026). URL https://amt.copernicus.org/articles/19/1245/2026/.

34. Clarisse, L., Van Damme, M., Clerbaux, C. & Coheur, P.-F. Tracking down global nh3 point sources with wind-adjusted superresolution. *Atmospheric Measurement Techniques* **12**, 5457–5473 (2019). URL https://amt.copernicus.org/articles/12/5457/2019/.

35. Frankenberg, C. *et al.* Airborne methane remote measurements reveal heavy-tail flux distribution in four corners region. *Proceedings of the National Academy of Sciences* **113**, 9734–9739 (2016). URL https://www.pnas.org/doi/abs/10.1073/pnas.1605617113. https://www.pnas.org/doi/pdf/10.1073/pnas.1605617113.

36. Varon, D. J. *et al.* Quantifying methane point sources from fine-scale satellite observations of atmospheric methane plumes. *Atmospheric Measurement Techniques* **11**, 5673–5686 (2018). URL https://amt.copernicus.org/articles/11/5673/2018/.

37. Molod, A. *et al.* The geos-5 atmospheric general circulation model: Mean climate and development from merra to fortuna. https://portal.nccs.nasa.gov/datashare/gmao/geos-fp/das/ (2012). Accessed: 12 June 2026.

38. Madhavan, S. & Sathe, S. Y. Inspection of ammonia plants. *Plant/Operations Progress* **6**, 35–41 (1987). URL https://aiche.onlinelibrary.wiley.com/doi/abs/10.1002/prsb.720060110. https://aiche.onlinelibrary.wiley.com/doi/pdf/10.1002/prsb.720060110.

39. World Bank. Environmental, health, and safety guidelines for nitrogenous fertilizer production. Tech. Rep., World Bank Group (2007). URL https://documents1.worldbank.org/curated/en/824921487313555203/pdf/112800-WP-ENGLISH-Nitrogenous-Fertilizers-PUBLIC.pdf. EHS Guidelines, accessed 2026-06-22.

40. Guanter, L. *et al.* Multisatellite data depicts a record-breaking methane leak from a well blowout. *Environmental Science & Technology Letters* **11**, 825–830 (2024). URL https://doi.org/10.1021/acs.estlett.4c00399. https://doi.org/10.1021/acs.estlett.4c00399.

41. Roger, J., Guanter, L., Gorroño, J. & Irakulis-Loitxate, I. Exploiting the entire near-infrared spectral range to improve the detection of methane plumes with high-resolution imaging spectrometers. *Atmospheric Measurement Techniques* **17**, 1333–1346 (2024). URL https://amt.copernicus.org/articles/17/1333/2024/.

42. Schuit, B. J. *et al.* Automated detection and monitoring of methane super-emitters using satellite data. *Atmospheric Chemistry and Physics* **23**, 9071–9098 (2023). URL https://acp.copernicus.org/articles/23/9071/2023/.

43. Goel, V. *et al.* Acidification potential estimation for small hydropower using lca methodology in india. *Scientific Reports* **15**, 5768 (2025). URL https://doi.org/10.1038/s41598-024-82397-5.

44. Alves, M. O., Nelson de Goes, L. M. & Simonelli, G. Impact on greenhouse gas emissions in the ammonia production process by reusing heat in the co2 absorption stage. *Energy Conversion and Management* **347**, 120534 (2026). URL https://www.sciencedirect.com/science/article/pii/S0196890425010581.

45. Green, R. O. *et al.* Imaging spectroscopy and the airborne visible/infrared imaging spectrometer (aviris). *Remote Sensing of Environment* **65**, 227–248 (1998). URL https://www.sciencedirect.com/science/article/pii/S0034425798000649.

46. Sánchez-García, E., Gorroño, J., Irakulis-Loitxate, I., Varon, D. J. & Guanter, L. Mapping methane plumes at very high spatial resolution with the worldview-3 satellite. *Atmospheric Measurement Techniques* **15**, 1657–1674 (2022). URL https://amt.copernicus.org/articles/15/1657/2022/.

47. Celesti, M. *et al.* The copernicus hyperspectral imaging mission for the environment (chime): Status and planning. In *IGARSS 2022 - 2022 IEEE International Geoscience and Remote Sensing Symposium*, 5011–5014 (2022).

48. Patterson, J. & Reina, F. Presentation 3263. Living Planet Symposium 2025, European Space Agency (ESA) (2025). URL https://lps25.esa.int/lps25-presentations/presentations/3263/_3263.pdf.

49. Bertin, T. *et al.* The hitran2024 methane update. *Journal of Quantitative Spectroscopy and Radiative Transfer* **349**, 109736 (2026). URL https://www.sciencedirect.com/science/article/pii/S002240732500398X.

50. Eriksson, P., Buehler, S., Davis, C., Emde, C. & Lemke, O. Arts, the atmospheric radiative transfer simulator, version 2. *Journal of Quantitative Spectroscopy and Radiative Transfer* **112**, 1551–1558 (2011). URL https://www.sciencedirect.com/science/article/pii/S0022407311001105.

51. Mayer, B. & Kylling, A. Technical note: The libradtran software package for radiative transfer calculations - description and examples of use. *Atmospheric Chemistry and Physics* **5**, 1855–1877 (2005). URL https://acp.copernicus.org/articles/5/1855/2005/.

Competing interests: The authors declare no competing interests.

List of Figures

1 Atmospheric transmittance spectra in the 1400 nm–2500 nm spectral range from H_2O (blue), CH_4 (orange), CO_2 (green), N_2O (purple), and NH_3 (red) that were extracted from combining HITRAN 2024[49], ARTS[50], and libRadtran[51] (Section S1). The ammonia default atmospheric concentration was multiplied by a factor of 5 for better visualization. Ammonia absorption features are divided into several spectral windows: 1500 nm (A), 1650 nm (B), 2000 nm (C), and 2300 nm (D). 16

2 Relationship between the wind speed at 10 m above surface (U_{10}), the retrieval noise (σ_{BG}), and the plume detection limit (Q_{det}). Q_{det} lines are overlaid in the plots for better interpretability. These relationships were established for EnMAP (left panel) and EMIT (right panel). 17

3 Examples of ammonia plumes overlaid on high-resolution Google Earth images. Starting from the top and from left to right, we find ammonia sources in Algeria (EMIT), Pakistan (MethaneSat), India (GF-5A AHSI), Uzbekistan (EnMAP), and Iraq (PRISMA). Details of the ammonia concentration-path length enhancement levels, acquisition date, source coordinates, and emission quantification for $\tau = \infty$ and $\tau = 1$ h can be found for each plume. . . . 18

4 Time-series of ammonia emissions from a fertilizer plant in Iraq during the time spanning between September 2023 to March 2026. Detections were marked as gray, and quantified emissions were marked as blue and red when considering $\tau = \infty$ and $\tau = 1$ h, respectively. Second-order polynomial fits along with their uncertainties for both τ values are also shown in the time series for both cases. Mean daily ammonia emission rate values are located at the upper part of the figure. 19

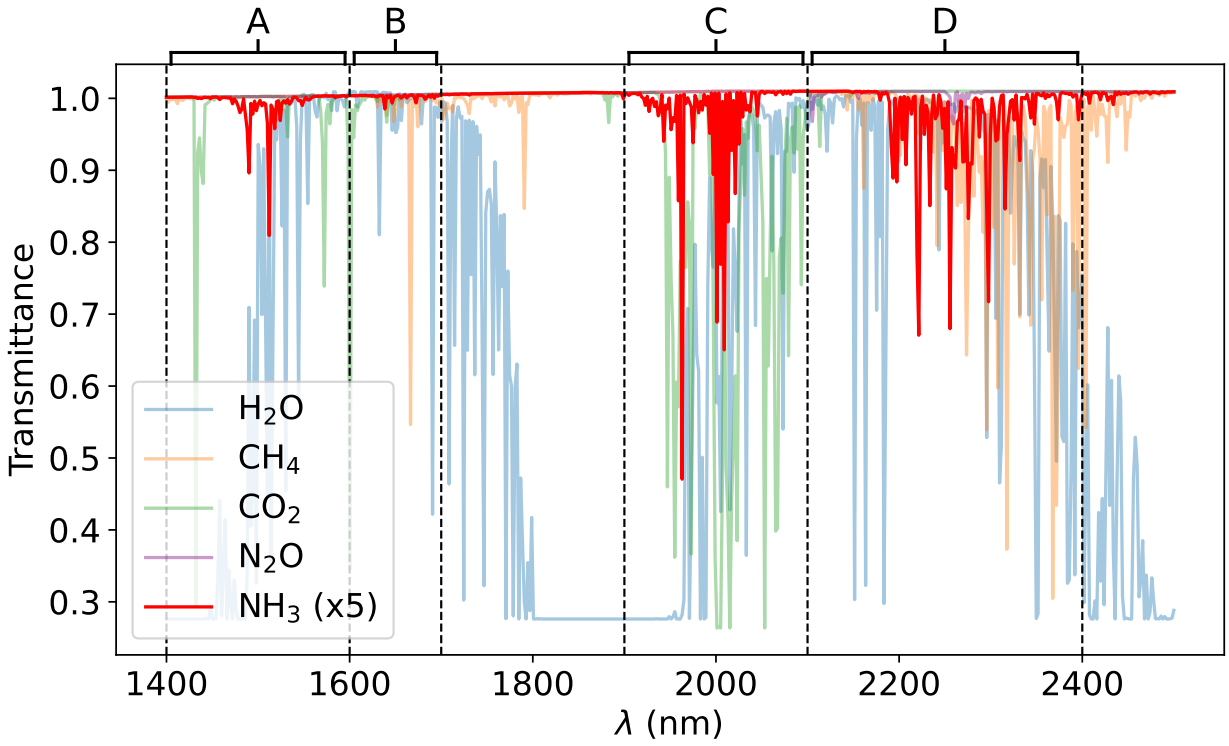

Figure 1: Atmospheric transmittance spectra in the 1400 nm–2500 nm spectral range from H_2O (blue), CH_4 (orange), CO_2 (green), N_2O (purple), and NH_3 (red) that were extracted from combining HITRAN 2024[49], ARTS[50], and libRadtran[51] (Section S1). The ammonia default atmospheric concentration was multiplied by a factor of 5 for better visualization. Ammonia absorption features are divided into several spectral windows: 1500 nm (A), 1650 nm (B), 2000 nm (C), and 2300 nm (D).

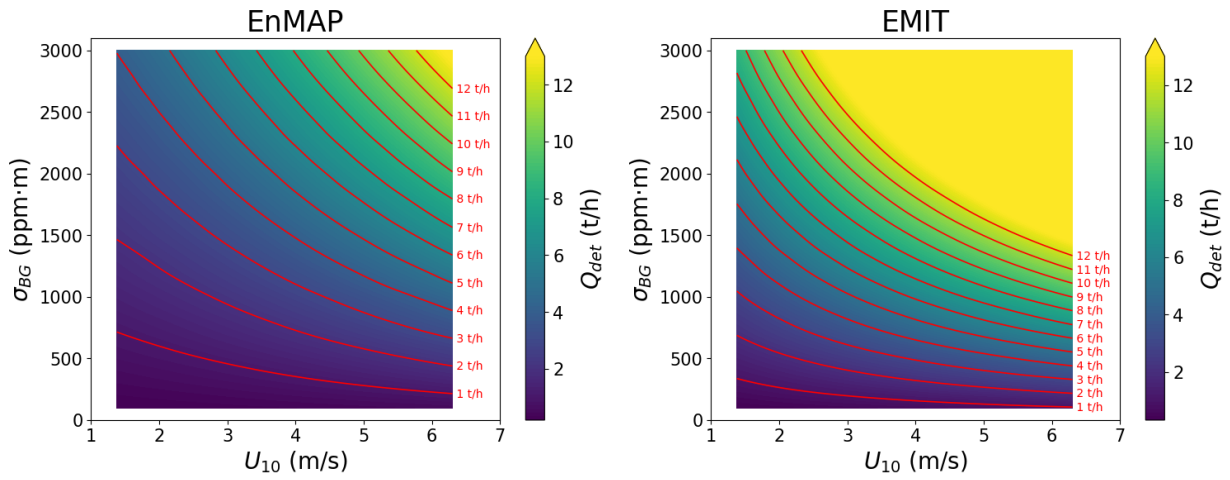

Figure 2: Relationship between the wind speed at 10 m above surface (U_{10}), the retrieval noise (σ_{BG}), and the plume detection limit (Q_{det}). Q_{det} lines are overlaid in the plots for better interpretability. These relationships were established for EnMAP (left panel) and EMIT (right panel).

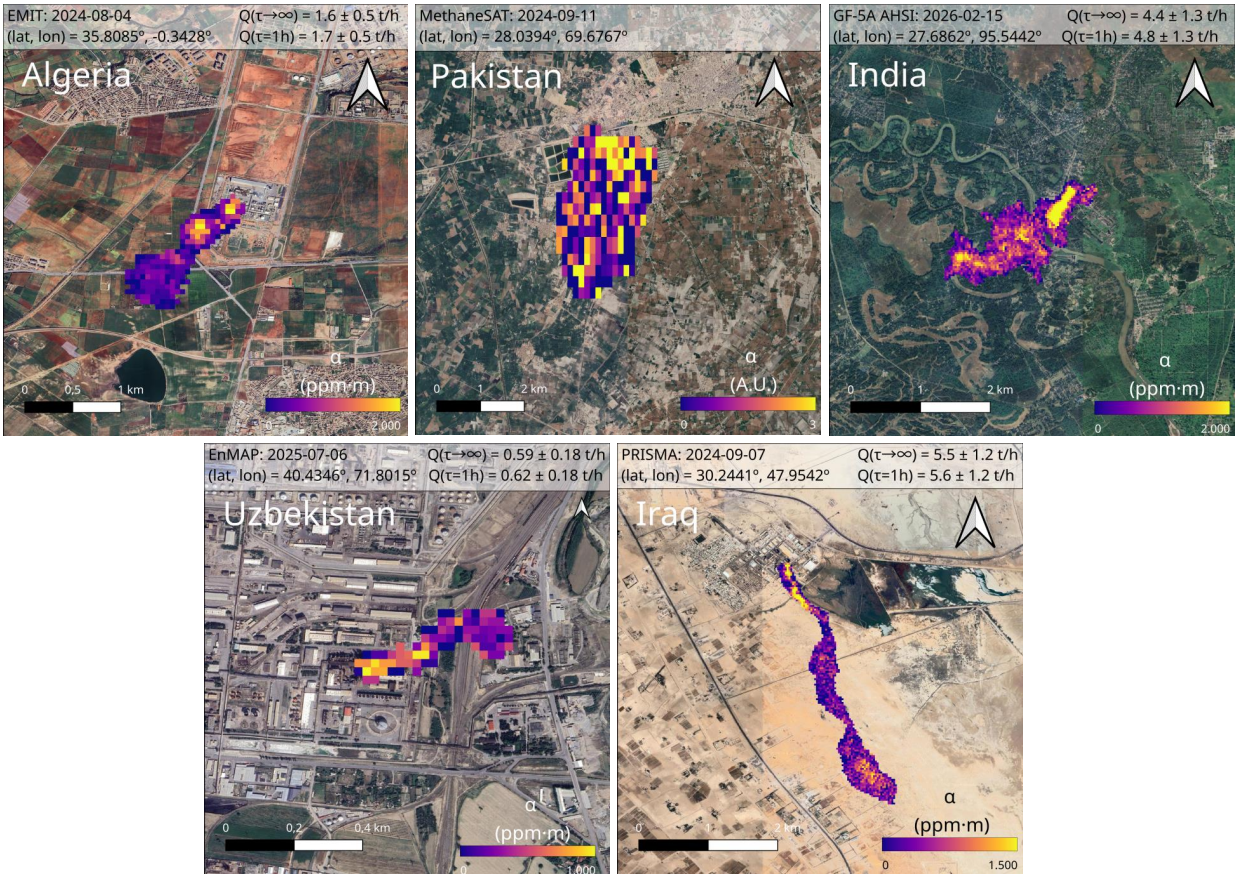

Figure 3: Examples of ammonia plumes overlaid on high-resolution Google Earth images. Starting from the top and from left to right, we find ammonia sources in Algeria (EMIT), Pakistan (MethaneSat), India (GF-5A AHSI), Uzbekistan (EnMAP), and Iraq (PRISMA). Details of the ammonia concentration-path length enhancement levels, acquisition date, source coordinates, and emission quantification for $\tau = \infty$ and $\tau = 1$ h can be found for each plume.

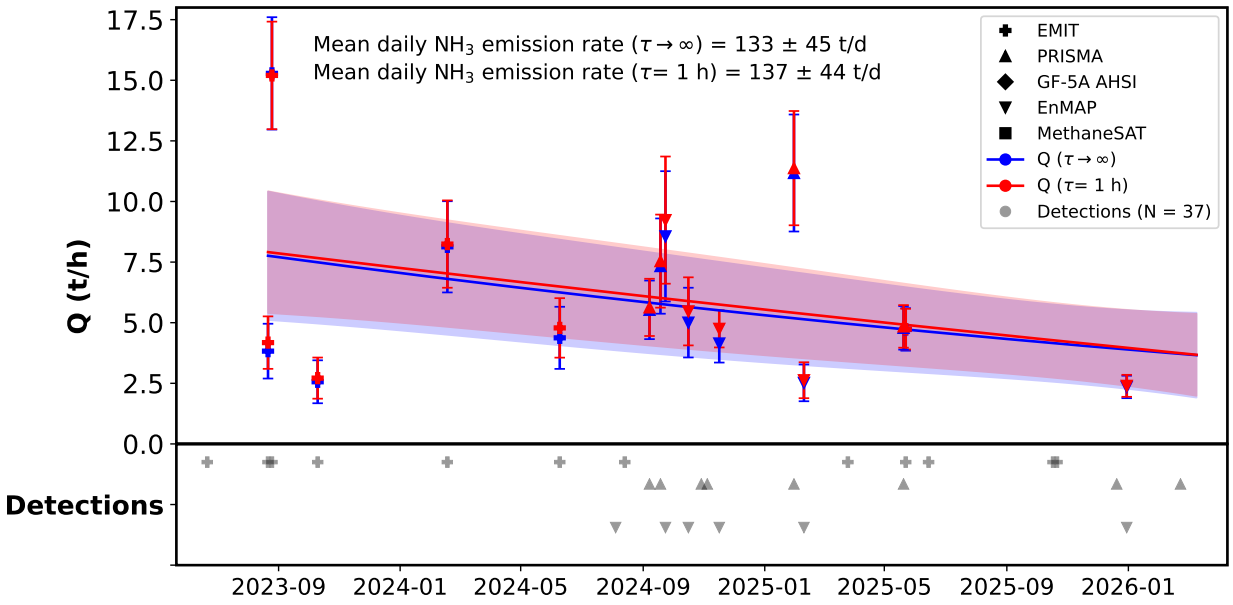

Figure 4: Time-series of ammonia emissions from a fertilizer plant in Iraq during the time spanning between September 2023 to March 2026. Detections were marked as gray, and quantified emissions were marked as blue and red when considering $\tau = \infty$ and $\tau = 1$ h, respectively. Second-order polynomial fits along with their uncertainties for both τ values are also shown in the time series for both cases. Mean daily ammonia emission rate values are located at the upper part of the figure.

Supplementary Materials

Remote sensing of ammonia point sources at high spatial resolution with satellite-based imaging spectrometers

Javier Roger[1,2*], Adriana Valverde[1], Javier Gorroño[1], Zhipeng Pei[3], Itziar Irakulis-Loitxate[1,4] Luis Guanter[1,5]

[1]Research Institute of Water and Environmental Engineering (IIAMA), Universitat Politècnica de València (UPV), Valencia, Spain.

[2]Now at: Institute of Environmental Physics (IUP), University of Bremen, Bremen, Germany.

[3]School of Remote Sensing and Information Engineering, Wuhan University, Wuhan, China.

[4]International Methane Emissions Observatory, United Nations Environment Programme.

[5]Environmental Defense Fund, Amsterdam, the Netherlands.

[*]To whom correspondence should be addressed; E-mail: jroger@iup.physik.uni-bremen.de

Contents

S1 Extraction of the gas unit absorption enhancement . . . 3
S2 Detection limit analysis . . . 4
S3 IME plume quantification: effective wind speed calibration . . . 10
S4 Ammonia retrieval in the 1500 nm and 2000 nm windows . . . 13
S5 Analyzing the correlation with other gases . . . 15
S6 Selection of the best retrieval for plume detection . . . 15
S7 Time-series assessment of a fertilizer plant in Iraq . . . 16

List of Tables

S1 List of all ammonia plume detections considered in this study . . . 5
S2 Retrieval noise in 'ideal' and 'not-ideal' locations for several instruments. . . . 6
S3 U_{eff} calibration parameters . . . 15

List of Figures

S1 Selection of the best polynomial fit for the U_{10} and Q_{det} relationship . . . 7
S2 Analysis of the U_{10} and Q_{det} relationship for different retrieval windows in an 'ideal' and 'not-ideal' cases . . . 8
S3 Detection limit results for several instruments . . . 9
S4 Assessment of the τ effect on the detection limit . . . 10
S5 Effective wind speed calibration for EnMAP and EMIT . . . 12
S6 Effective wind speed calibration for PRISMA . . . 13
S7 Analysis of plume detection on several retrieval windows . . . 14
S8 Analysis of potential emission correlation with other gas retrievals . . . 17
S9 Assessment of the WWMF retrieval performance . . . 18
S10 Selection of the best polynomial fit for time-series of the Iraq fertilizer plant . . . 19

S1 Extraction of the gas unit absorption enhancement

Assuming a default midlatitude summer atmosphere extracted from the RFM model (*1*), HITRAN 2024 (*2*) lines from a set of gases were processed through ARTS (*3*) to calculate the optical depth vertical profile spectra, to which water vapor continuum absorption from the MT_CKD (*4*) model was added. The resulting optical depth was introduced as input for libRadtran (*5*) to compute radiance spectra under specific conditions at a 0.1 nm spectral sampling. In our atmosphere, we included the following gases: CH_4, CO_2, H_2O, O_3, O_2, N_2O, CO, and NH_3. We assumed surface at sea level, a water vapor content of 3 cm, and gas enhancements were considered in the first 500 m above surface. Following this procedure, we generated a lookup table (LUT) of radiance spectra for a range of gas enhancement values and geometrical air mass factors. These spectra were used to calculate the unit gas absorption spectrum (K) as in Foote et al. (*6*), which is needed to run the matched filter method.

We set the following atmospheric concentrations: XCH_4 = 1.875 ppm, XCO_2 = 410 ppm, XN_2O = 0.340 ppm, XCO = 0.1 ppm, and XNH_3 = 0.05 ppm, XH_2O = 3 cm. O_3 and O_2 concentrations were set to the default concentrations from the RFM model. Moreover, we set the following range of concentration values: $\alpha(CH_4)$ = [0, 20000] ppm·m, $\alpha(CO_2)$ = [0, 1280000] ppm·m, XH_2O = [0, 5] cm, and $\alpha(NH_3)$ = [0, 2697] ppm·m. These values were selected to represent realistic gas atmospheric concentrations and typical variation from trace gases.

$\alpha(CH_4)$ and $\alpha(CO_2)$ ranges were selected in this manner since pixels from these gas plumes captured with EMIT, EnMAP, PRISMA, and GF-5A AHSI are typically within these values. Regarding XH_2O values, we just set typical atmospheric values in reference to our default in order to check correlation with ammonia plumes. In order to obtain a realistic $\alpha(NH_3)$ range, we used a similar approach to Section S2 to get the emission rate at which a plume could be detected. This approach first requires adding random noise to the simulated plumes. At this point, we do not have examples of retrieval noise. We therefore propagate the EnMAP and EMIT instrument noise (*7, 8*) to retrieval noise values similarly to Roger et al. (*9*). The resulting values do not consider the surface-related noise and other instrument effects, which yields an optimistic estimation of the retrieval noise values. Nevertheless, we consider this estimation valid enough to obtain a representative range of $\alpha(NH_3)$ values.

As for the ammonia atmospheric concentrations, there is high variability of this value across time and location. However, our main targets are fertilizer plants, which operate with practically no interruptions (*10*). Assuming frequent emissions, concentrations over our targets are probably higher than in other areas. According to ATSDR et al. (*11*), XNH_3 values near industrial sites in Germany ranged from 0.01 to 0.09 ppm. We select a value of 0.05 ppm, matching the mean value within this range.

S2 Detection limit analysis

We carry out a sensitivity analysis to assess the ammonia plume detection limit using the EnMAP and EMIT instruments. For this purpose, we combine random noise with synthetic plumes to reproduce realistic ammonia concentration-path length enhancement maps (α) in ppm·m units.

Random noise is extracted from 1-standard deviation of ammonia retrievals (σ_{BG}) using EnMAP and EMIT data under the 3 main fitting windows, i.e. those around 2300 nm, 1500 nm, and 2000 nm (see Figure 1). Specifically, we used acquisitions capturing the same areas from Iraq and Bangladesh locations (Table S1) where emissions from fertilizer plants were detected. While the Iraq acquisition reflects a bright scene in a desertic region, the Bangladesh acquisition shows a darker scene with vegetation. The selections of these 2 areas were made to account for an 'ideal' (Iraq) and a 'not-ideal' (Bangladesh) scenarios for detection in the sensitivity analysis. The selected acquisitions along to the related retrieval noise are listed in Table S2.

Synthetic plumes are obtained from the WRF-LES database accessible in (*12*) and described in Gorroño et al., (*13*), which contain 3D point source emissions for 11 geostrophic winds (ranging between 2 m/s and 10 m/s) at 20m spatial resolution. Each has a duration of 1 h with a temporal difference of 60 seconds between snapshots, although we selected one snapshot every 120 s to reduce plume shape correlation (Ouerghi et al., 2025). We collapsed the 3D simulations into 2-D ammonia α maps with a fixed instrument angular configuration of VZA = 0º, SZA = 30º, and RAA = 90º. These angles were selected based on existing EnMAP and EMIT acquisitions (Roger et al., 2025). Under the assumption of linearity between α values and emission rate, we can change the original plume emission rate by simply scaling the map. Moreover, even though these simulations were originally designed for methane, we adapt it to the ammonia case by just changing the gas molar mass.

Once we obtain the α maps, we downsample them to the pixel size of 30 m and 60 m, which are related to the ground sampling distance of EnMAP and EMIT, respectively. Next, we add Gaussian noise related to the ammonia retrievals extracted from the instrument acquisitions. Then, an iterative methodology is applied, where we increase the plume emission rate with steps of 0.1 t/h until the plume is detected. This method is very similar to the one used in Roger et al. (2025), except that α maps are not obtained by implementing simulated plumes into L1 acquisitions. That study was carried out in offshore areas, where there is usually a high spectral homogeneity and low number of retrieval artifacts. These conditions allowed for an automatization of the procedure and a generalization of the results. Since ammonia sources are typically located in in-land areas, we avoid this approach. Instead, we use those maps resulting from simply combining the collapsed synthetic plumes and realistic noise from ammonia retrievals. The main downside of this alternative are the potential accuracy deficiencies in the matched filter retrievals, which would change the SNR of the plume (Roger et al., 2024b). However, we consider this approach as a first approximation that can be improved in further research.

Table S1: List of all ammonia plume detections considered in this study. Every row shows an emission detection, but not all of them were suitable for quantification. Acquisitions with no emission detection were discarded. Those emissions that did not pass a quality screening for quantification were marked with "–".

Site	Mission	Timestamp (YYYYMMDD)	Source-lat (°)	Source-lon (°)	U_{10} (m/s)	$Q_{\tau=\infty}$ (kg/h)	err($Q_{\tau=\infty}$) (kg/h)	$Q_{\tau=1h}$ (kg/h)	err($Q_{\tau=1h}$) (kg/h)
Uzbekistan	GF-5A AHSI	20240807	40.4329	71.8030	4.61	1939.21	628.63	2030.97	614.59
Uzbekistan	GF-5A AHSI	20240807	40.4402	71.8224	4.61	4352.04	1399.37	4557.97	1366.47
Uzbekistan	EnMAP	20250706	40.4346	71.8015	5.52	592.38	179.52	615.07	176.91
Iran	EMIT	20231006	35.4256	53.2163	5.12	1855.15	570.2	1913.44	547.27
Pakistan	PRISMA	20240415	28.0289	69.6570	2.25	824.63	255.6	891.39	250.3
Pakistan	EnMAP	20241120	28.0423	69.6761	1.26	1325.96	290.85	1498.71	284.24
Pakistan	MethaneSAT	20240911	28.0394	69.6767	-	-	-	-	-
India	GF-5A AHSI	20260215	27.1791	95.3518	2.21	4363.12	1259.07	4764.89	1229.31
India	EnMAP	20250528	27.1802	95.3525	3.78	2102.77	738.8	2225.22	721.63
Algeria	EMIT	20240804	35.8085	-0.3428	2.37	1568.88	482.18	1700.82	461.77
Iraq	EMIT	20251021	30.1878	47.8269	-	-	-	-	-
Iraq	EMIT	20230621	30.1888	47.8278	-	-	-	-	-
Iraq	EMIT	20250522	30.1807	47.8441	9.36	4722.33	876.35	4734.1	839.62
Iraq	EMIT	20230821	30.1878	47.8381	2.15	3826.97	1130	4178.77	1082.04
Iraq	EMIT	20240813	30.1865	47.8393	-	-	-	-	-
Iraq	EMIT	20251017	30.1856	47.8334	-	-	-	-	-
Iraq	EMIT	20231010	30.1894	47.8342	3.32	2563.22	885.75	2714.66	848.27
Iraq	EMIT	20240217	30.1882	47.8360	7.16	8129.65	1881.47	8243.16	1801.64
Iraq	EMIT	20230825	30.1881	47.8283	11.72	15284.39	2317.06	15199.72	2218.68
Iraq	EMIT	20250325	30.1851	47.8388	-	-	-	-	-
Iraq	EMIT	20250614	30.1869	47.8258	-	-	-	-	-
Iraq	EMIT	20240609	30.1861	47.8365	2.1	4375.82	1280.86	4785.4	1226.47
Iraq	PRISMA	20241029	30.1522	47.7631	-	-	-	-	-
Iraq	PRISMA	20240918	30.1751	47.8186	6.05	7335.81	1965.04	7540.17	1919.44
Iraq	PRISMA	20260222	30.1006	47.6668	-	-	-	-	-
Iraq	PRISMA	20250520	30.1801	47.8250	9.29	4787.97	898.59	4847.42	877.98
Iraq	PRISMA	20241104	30.1476	47.7545	4.36	5635.01	1952.2	5876.54	1906.9
Iraq	PRISMA	20250130	30.1672	47.7968	7.85	11174.56	2412.8	11375.04	2356.81
Iraq	PRISMA	20240907	30.2441	47.9542	7.76	5530.37	1207.98	5631.94	1180.08
Iraq	PRISMA	20251220	30.1771	47.8164	3.32	2451.2	860.13	2591.83	840.41
Iraq	GF-5A AHSI	20251121	30.1784	47.8471	7.02	2480.11	576.96	2548.31	563.52
Iraq	GF-5A AHSI	20250410	30.1784	47.8373	7.7	2248.21	491.2	2301.62	480.36
Iraq	GF-5A AHSI	20241108	30.1767	47.8446	8.26	6306.78	1280.41	6439.76	1250.19
Iraq	GF-5A AHSI	20250910	30.1875	47.8435	8.2	4909.33	1001.55	5014.04	977.88
Iraq	GF-5A AHSI	20260310	30.1805	47.8427	4.53	4834.77	1572.73	5068.14	1535.36
Iraq	GF-5A AHSI	20241229	30.1777	47.8464	3.51	3192.48	1093.22	3392.36	1067.34
Iraq	GF-5A AHSI	20241222	30.1818	47.8346	4.76	3820.39	1199.36	3995.03	1170.96
Iraq	EnMAP	20240804	30.1852	47.8391	7.97	1959.04	413.59	2003.01	404.19
Iraq	EnMAP	20251230	30.1861	47.8396	8.63	2350.84	464.08	2396.54	453.5
Iraq	EnMAP	20241016	30.1876	47.8367	2.19	5004.07	1437.95	5467.78	1403.77
Iraq	EnMAP	20241116	30.1882	47.8368	0.99	4143.38	787.22	4748.26	768.56
Iraq	EnMAP	20240923	30.1869	47.8348	2.73	8562.57	2687.05	9231.83	2623.11
Iraq	EnMAP	20250209	30.1868	47.8390	5.03	2518.97	758.8	2626.88	740.93
Iraq	MethaneSAT	20250611	30.1860	47.8370	-	-	-	-	-
Iraq	MethaneSAT	20241106	30.1860	47.8370	-	-	-	-	-
Iraq	MethaneSAT	20240925	30.1860	47.8370	-	-	-	-	-
Iraq	MethaneSAT	20240911	30.1860	47.8370	-	-	-	-	-
Borneo	EMIT	20260126	0.1878	117.4764	3.04	1805.03	607.8	1922.94	582.37
Bangladesh	EMIT	20241202	24.6522	91.9425	2.18	3233.01	962.49	3526.75	922.37
China	EMIT	20250611	39.2482	111.1501	7.01	1690.61	417.93	1715.87	402.49

Table S2: Retrieval noise in 'ideal' and 'not-ideal' locations for several instruments.

Site	Mission	Timestamp (YYYYMMDD)	σ_{BG} (2300nm) (ppm·m)	σ_{BG} (1500nm) (ppm·m)	σ_{BG} (2000nm) (ppm·m)
Bangladesh	EnMAP	20251114	453.58	1152.54	2563.77
Bangladesh	EMIT	20241202	272.56	653.80	1465.99
Bangladesh	PRISMA	20201203	798.59	1854.89	3502.09
India	GF-5A AHSI	20260215	406.74	1052.80	1271.01
India	PRISMA	20210204	659.76	1513.96	2989.10
Iraq	PRISMA	20260222	272.62	740.78	1373.05
Iraq	GF-5A AHSI	20241222	275.45	569.92	1398.49
Iraq	EnMAP	20250205	216.74	641.98	1303.39
Iraq	EMIT	20230825	138.60	315.56	570.15

Following this iterative methodology, we obtain for each σ_{BG} value a set of $\{Q_{\mathrm{det}}, U_{10}\}$ values, i.e. Q_{det} is the minimum emission rate at which the plume can be detected and U_{10} is the related wind speed at 10 m above surface, which was averaged over the whole plume domain and over the previous 10 minutes as in Gorroño et al. (2026). Next, we attempt to fit these data sets into polynomial functions. In Figure S1, we show a series of polynomial fits of 1st to 4th-order related to the results extracted for the EnMAP (left) and EMIT (right) instruments with σ_{BG} of 300 ppm·m (blue) and 1000 ppm·m (red). For the EMIT case, we observe that there is agreement for the polynomial fits of 1st to 3rd-order and reproduce quite well the increasing trend of the points. On the other hand, the one of 4th-order exhibits several inflection points that overfit the scattering of the data, even assuming a decreasing trend at higher wind speed values, which is not physically consistent. Regarding the EnMAP case, more discrepancy among the different fits is observed. We discard the polynomials of 3rd and 4th-order because they are more sensitive to scattering. The polynomial of 1st-order is also discarded because it does not account for the potential non-linearity in the $\{U_{10}, Q_{\mathrm{det}}\}$ relationship. Therefore, we select the polynomials of 2nd-order to fit our data from both instruments, which exhibit very similar values of root mean square error (RMSE) and the Pearson correlation coefficient (r) to the fits with best statistics. We observed that the fraction of points with Q_{det} higher than its related fitted value ranges within 40% and 48% depending on the noise level, which in turn makes the fitted curve representative of the emission rate at which we can detect approximately half of the plumes.

In Figure S2, we show the resulting curves for EnMAP (left) and EMIT (right) instruments based on the noise levels from the 3 fitting windows in the Iraq (blue) and Bangladesh (red) areas. We observe that EnMAP generally exhibits a more favorable detection limit, even though the σ_{BG} values are higher. This emphasizes the importance of a finer spatial resolution for plume detection. However, there are some exceptions to this conclusion. In the Iraq case, EMIT exhibits more favorable detection limits in the 1500 nm window at $U_{10} > 6$ m/s and in the 2000 nm window at $U_{10} < 2$ m/s and $U_{10} > 4$ m/s. While

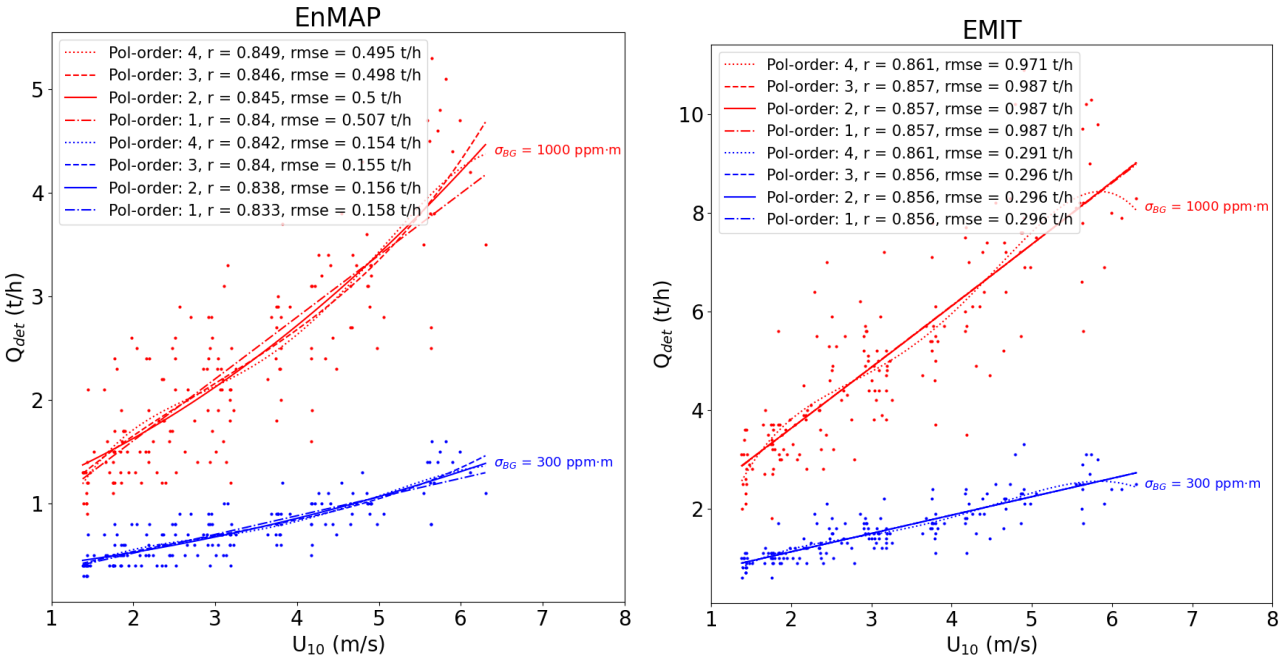

Figure S1: Data points showing the relationship between U_{10} and Q_{det}, fitted with polynomial curves of different orders (1st to 4th) for retrieval noise levels of 300 ppm·m (blue) and 1000 ppm·m (red). The left panel shows the EnMAP case, and the right panel the EMIT case. Fit statistics are included in the legend.

EnMAP curves exhibit concavity, the EMIT ones are more linear. This different behaviour makes both curves intersect at some points where the difference in background levels and spatial resolution does not lead to a significant difference in detection limit. For both instruments, the 2300 nm window provides the lowest detection limit, while the 2000 nm provides the highest ones. The difference between these two windows grows bigger in the Bangladesh case, which is considered a 'not-ideal' area. For instance, at 6 m/s we see a large detection limit difference of approximately 9 t/h and 10 t/h for EnMAP and EMIT in this area, respectively. On the other hand, the 1500 nm window yields detection limits in between the other two. This makes the 1500 nm window the best alternative to quality-check potential ammonia plume candidates extracted using the 2300 nm window. For Iraq, we have a minimum detection limit of 0.5 t/h and 0.8 t/h for EnMAP and EMIT, respectively. For Bangladesh, it increases to 1.1 t/h and 1.5 t/h for EnMAP and EMIT, respectively.

We consider that the 2300 nm window is the main spectral range that should be used for ammonia plume detection, but also for emission quantification. The higher plume SNR in the α maps makes the plume pixels less contaminated by noise, which ultimately has a positive impact on quantification.

Roger et al. (2024b) proposed a matched-filter methane retrieval methodology that exploited a wide spectral window to improve plume detection performance. When expanding the window to this range, it resulted in an over-penalization of the α values, in turn leading to a large underestimation of plume

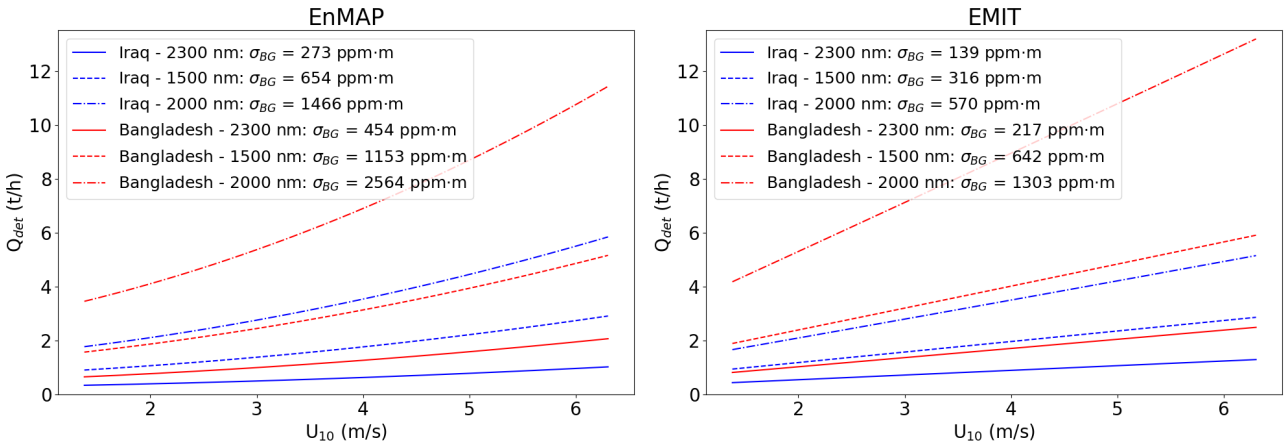

Figure S2: Fits showing the relationship between U_{10} and Q_{det} for the Iraq (blue) and Bangladesh (red) sources using different retrieval windows. The left panel shows the EnMAP case, and the right panel the EMIT case.

pixel values. Therefore, we did not include it into the sensitivity analysis. However, later in the text (Section S6) we will compare retrievals using this wide window to those applying the one of 2300 nm and visually assess whether there is an improvement for detection.

Now, we run the iterative method for a larger array of σ_{BG} values ranging from 100 ppm·m to 3000 ppm·m, separated by 100 ppm·m steps. We choose this range because it is wide enough to cover the σ_{BG} values from the previously analyzed acquisitions, which in turn represents 'ideal' and 'not-ideal' cases from both instruments. Then, we interpolate all the curves resulting from each noise level to generate a continuous 2D field that relates Q_{det}, U_{10}, and σ_{BG}. The results are shown in Figure S3, where we show the results for the EnMAP (left) and EMIT (right) instruments. The EnMAP results are also valid for those instruments with identical pixel size such as PRISMA, GF-5A AHSI, and Tanager-1. Nevertheless, Tanager-1 is likely to achieve lower retrieval noise, which may place it outside the retrieval noise range explored for EnMAP.

So far, we have not accounted for the relatively short lifetime of ammonia, which is significantly variable (Van Damme et al., 2018). The lifetime (τ) highly depends on several factors such as bidirectional ammonia atmosphere-surface fluxes and atmospheric composition. We previously extracted results assuming $\tau \to \infty$, as it is considered for methane and carbon dioxide. However, we want to understand how these results change when assuming more realistic τ values for ammonia.

We assume an exponential ammonia concentration decay:

$$\alpha(t) = \alpha(t=0) \cdot \exp(-t/\tau) \tag{1}$$

, where $\alpha(t)$ is the ammonia concentration-path length enhancement at time t, which represents the time after an ammonia particle is released from the source. We assume that the distance traveled by

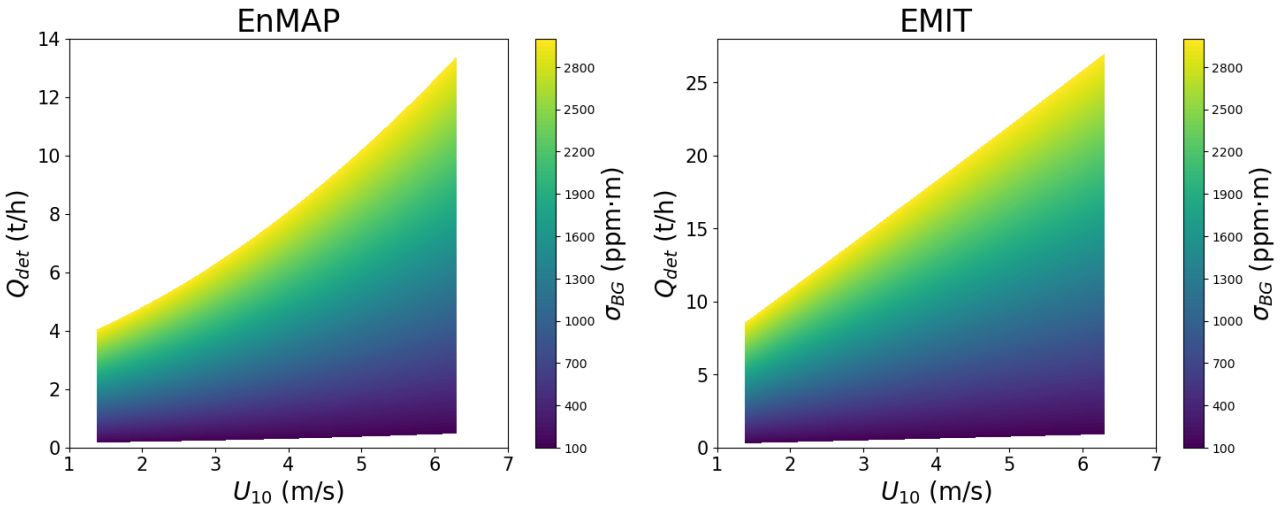

Figure S3: Relationship between the wind speed at 10 m above the surface (U_{10}), the retrieval noise (σ_{BG}), and the plume detection limit (Q_{det}). These relationships were established for EnMAP (left panel) and EMIT (right panel).

the particles contained in a given pixel is equal to the Euclidean distance between that pixel and the source pixel. We also assume that these particles move following a constant wind speed, which can be approximated by the plume-related U_{10} value. In this manner, we can obtain t using the following expression:

$$t = \frac{d}{U_{10}} \tag{2}$$

$$d = \sqrt{(\mathrm{GSD} \cdot N_x)^2 + (\mathrm{GSD} \cdot N_y)^2} \tag{3}$$

, where GSD is the ground sampling distance (approximately pixel size), and N_x and N_y are the number of pixels from the source to a given pixel in the horizontal and vertical projections of the α map, respectively. These assumptions ignore factors such as temporal and spatial variability of wind speed at smaller scales, which in turn affect the real distance traveled by each particle. We acknowledge that more complex simulations that account for all interactions of ammonia with the environment under specific conditions would provide more accurate results. Nevertheless, we consider this a first-order approach to account for the decay in concentration of short-lived gases with finite lifetimes. For our analysis, we considered $\tau = 1$ h, 12 h, and 48 h as in Van Damme et al. (*14*), since this represents most of the ammonia lifetime variability according to existing literature.

We obtained detection limit results for the Iraq area considering the EnMAP and EMIT instruments for different τ values. In order to compare with the previously obtained results, we used a relative

difference (ε), defined as:

$$\varepsilon = \frac{Q_{\tau\to\infty} - Q_{\tau=Xh}}{Q_{\tau\to\infty}} \cdot 100 \tag{4}$$

, where $Q_{\tau\to\infty}$ and $Q_{\tau=Xh}$ are the detection limit results considering an infinite lifetime and a lifetime of X hours, respectively. We mostly obtained negative values of ε, as the decay in ammonia concentration challenges plume detection and therefore leads to higher detection limits. While for $\tau = 12$ h and $\tau = 48$ h ε did not get lower than -1%, for $\tau = 1$ h ε reached -6% and -8% for the EnMAP and EMIT instruments, respectively (Figure S4). These larger differences happen especially at lower U_{10} values because it takes more time for ammonia particles to move, and a more pronounced decay near the source takes place. Altogether, the previously obtained detection limit values ($Q_{\tau\to\infty}$) will be very similar to the ones with τ as low as 12 h, while detection limits for $\tau = 1$ h will be slightly higher, especially for low U_{10} values. Nevertheless, we do not consider the difference significant enough to run the iterative algorithm for $\tau = 1$ h. Instead, we consider that Figure S3 can be approximately generalized for the analyzed range of τ values.

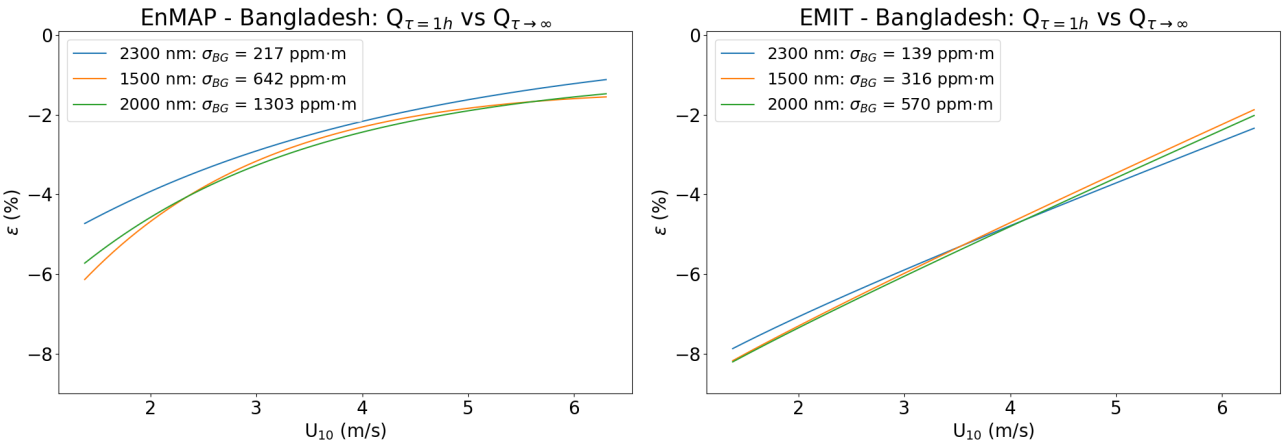

Figure S4: Relative difference (ε) between the detection limit considering $\tau \to \infty$ and $\tau = 1$ h in Iraq for the 2300 nm (blue), 1500 nm (orange), and 2000 nm (green) absorption windows. The left panel shows the EnMAP case, and the right panel the EMIT case.

S3 IME plume quantification: effective wind speed calibration

We quantify ammonia point source emissions based on the IME quantification method (Frankenberg et al., 2016), which is formulated as follows:

$$Q = \frac{\mathrm{IME} \cdot U_{\mathrm{eff}}}{L} \tag{5}$$

, where Q is the emission rate (t/h), IME is the integrated mass enhancement (kg) of the emission, L is the plume size (m), and U_{eff} is the effective wind speed. Plume size is calculated from the square root of the plume area, which is obtained through a manual delineation over the α map.

The IME is calculated as follows:

$$\text{IME} = \frac{\text{GSD}^2 \cdot M_{\text{NH}_3} \cdot \Delta p \cdot \sum_i (\alpha_i)}{g \cdot M_{\text{air}} \cdot H} \tag{6}$$

with:

$$\text{GSD(EnMAP)} = 30 \text{ m} \tag{7}$$

$$\text{GSD(EMIT)} = 60 \text{ m} \tag{8}$$

$$M_{\text{NH3}} = 17.0305 \text{ g/mol} \tag{9}$$

$$M_{\text{air}} = 28.9644 \text{ g/mol} \tag{10}$$

$$g = 9.8067 \text{ m/s}^2 \tag{11}$$

, where M_{NH_3} and M_{air} are the molar mass of ammonia and dry air, respectively; g is the acceleration of gravity on Earth; and H is the thickness of the lowest atmospheric layer where the ammonia enhancement is assumed. We assumed $H = 500$ m as in Foote et al. (2021), and we extract Δp from the same atmosphere we considered for the extraction of the ammonia unit absorption spectra. For this study, we selected a default midlatitude summer atmosphere based on the RFM model (Dudhia et al., 2017).

Moreover, we extract the effective wind speed (U_{eff}) similarly to Guanter et al. (2024) by using the same WRF-LES data set we employed for the detection limit study. Values of $\tau = 1$ h, 12 h, 48 h, and $\tau \to \infty$ are again considered.

We need to select a range of values for the emission rate and retrieval background noise to deduce U_{eff}. Since the 2300 nm window was identified as the most suitable spectral range for quantification, for each instrument we defined a 10-value noise array spanning the noise levels between the 'ideal' (Iraq) and 'non-ideal' (Bangladesh) scenes within this window. Regarding the emission rate, we define another 10-value array ranging from 0.1 t/h to 5 t/h. Combined with the selected range of noise levels, it covers a significant variety of plumes that are mostly over the detection limit. Nevertheless, those plumes below the detection limit are not taken into account.

In Figure S5, we show the U_{eff} values for the EnMAP (left) and EMIT (right) cases for different lifetime values. U_{eff} values for $\tau = 48$ h and $\tau = 12$ h are very similar to those of $\tau \to \infty$. On the other hand, U_{eff} values for $\tau = 1$ h are higher as a larger reduction of ammonia concentration must be compensated. For this case, we observe a larger intercept and slight reduction in the slope. Similarly to the detection limit study, this matches with the highest difference at low wind speed values, while

it narrows down at higher wind speed values. Moreover, the slightly higher detection limit when considering $\tau = 1h$ leads to more scattered points at low noise levels, which also has an impact in the U_{eff} fit.

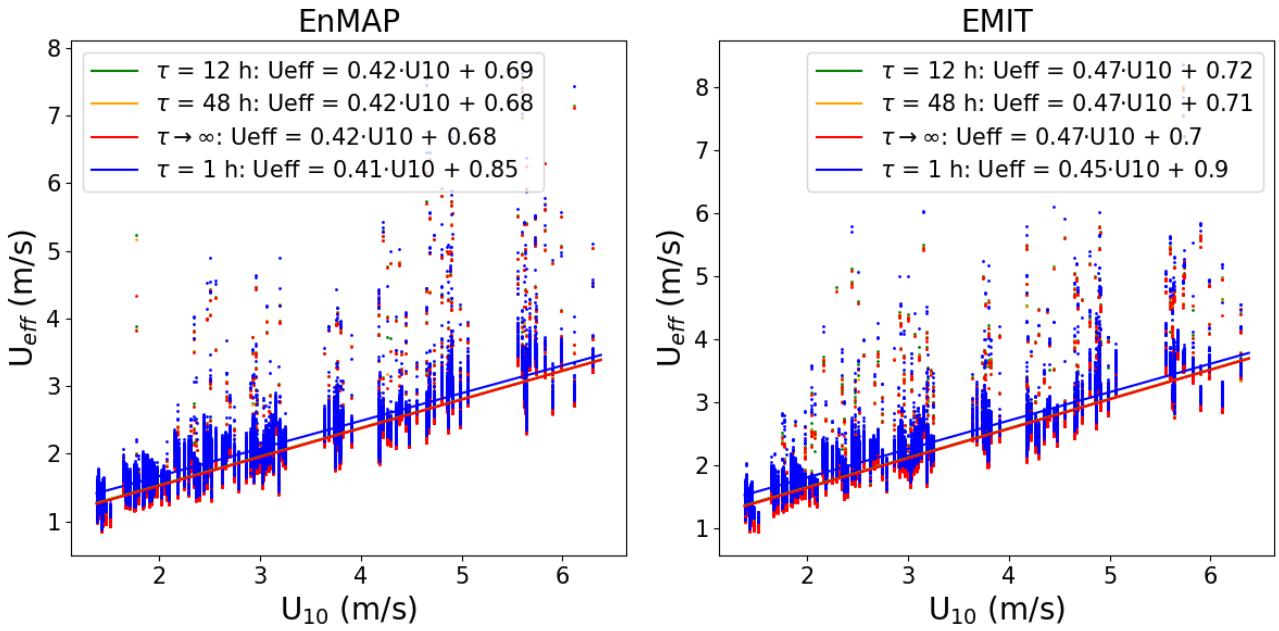

Figure S5: U_{eff} calibrations for IME plume quantification considering $\tau \to \infty$ (red), $\tau = 1$ h (blue), $\tau = 12$ h (green), and $\tau = 48$ h (orange). The left panel shows the EnMAP case, and the right panel the EMIT case.

Since we also detected ammonia plumes using GF-5A AHSI and PRISMA data, the effective wind speed calibration for these instruments is also required for plume quantification. For both instruments, we could obtain acquisitions in the Iraq area, which is our reference for an 'ideal' case. While we could also obtain a PRISMA acquisition from the Bangladesh area ('not-ideal' case), this was not possible for the GF-5A AHSI instrument. Instead, we used an acquisition from an India area, where we identified an ammonia plume. This area is similar to that of Bangladesh since it exhibits a relatively low albedo. We found that GF-5A AHSI exhibits similar retrieval noise values to those of EnMAP for both the 'ideal' and 'not-ideal' cases. On the other hand, while PRISMA 'ideal' noise is also similar to that of EnMAP and GF-5A AHSI, the 'not-ideal' case shows a significantly higher retrieval noise. In order to verify that the difference in retrieval noise for the 'not-ideal' case was not due to the different area selection, we additionally extracted the retrieval noise for PRISMA in the India area. We also obtained a similar difference, which confirmed the correct selection of the new area. Therefore, we can approximate the GF-5A AHSI effective wind speed calibration to that of EnMAP, but we must compute another calibration for PRISMA taking into account the new range of retrieval noise values. We show the resulting effective wind speed calibration in Figure S6. This is only illustrated for $\tau = 1$ h and $\tau \to \infty$, since we already saw that the results from $\tau = 12$ h and $\tau = 48$ h are very similar to those

from $\tau \rightarrow \infty$. Information about these new acquisitions along with their related retrieval noise can also be found in Table S2. Moreover, the list of instrument-specific U_{eff} calibration parameters is listed in Table S3.

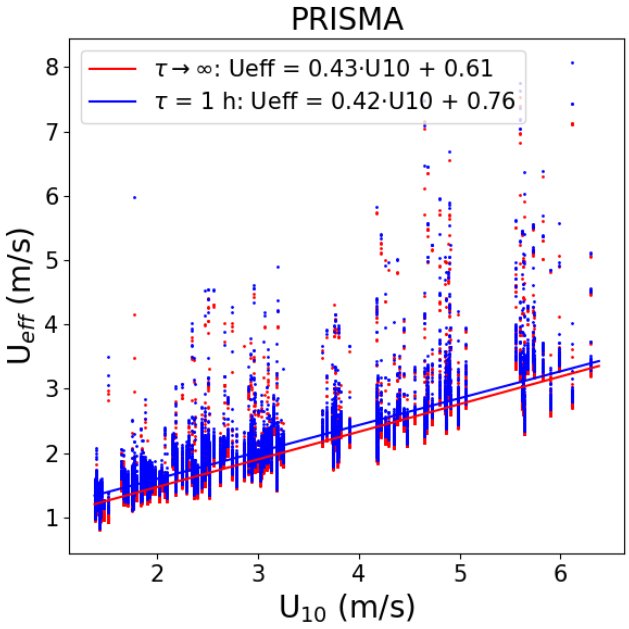

Figure S6: U_{eff} calibration for IME plume quantification considering $\tau \rightarrow \infty$ (red) and $\tau = 1$ h (blue) for the PRISMA instrument.

S4 Ammonia retrieval in the 1500 nm and 2000 nm windows

The ammonia retrieval based on the 2300 nm window was selected as the main window to detect and quantify emissions due to its lowest SNR. We also extract the retrievals using the 1500 nm and 2000 nm windows for the emissions shown in the main part of the manuscript to assess whether the ammonia plume can also be seen using these retrievals, which would be a strong indicator of a true detection. In Figures S7, we show the unmasked ammonia retrievals of those emissions shown in Figure 3, except for the MethaneSAT case since it does not cover these spectral ranges.

For the EnMAP case, we could only see the plume in the 2300 nm window, which is consistent with the increasing noise in the other retrievals and the relatively low emission rate of the plume. For the PRISMA case, the strongest part of the plume tail is somewhat visible in the 1500 nm retrieval, while the 2000 nm retrieval is dominated by noise. The surface beneath the plume seems to positively score in the matched filter retrieval, which challenges the detection. For the GF-5A AHSI and EMIT cases, the plumes are visible in the three retrievals, with a significantly more challenging detection in

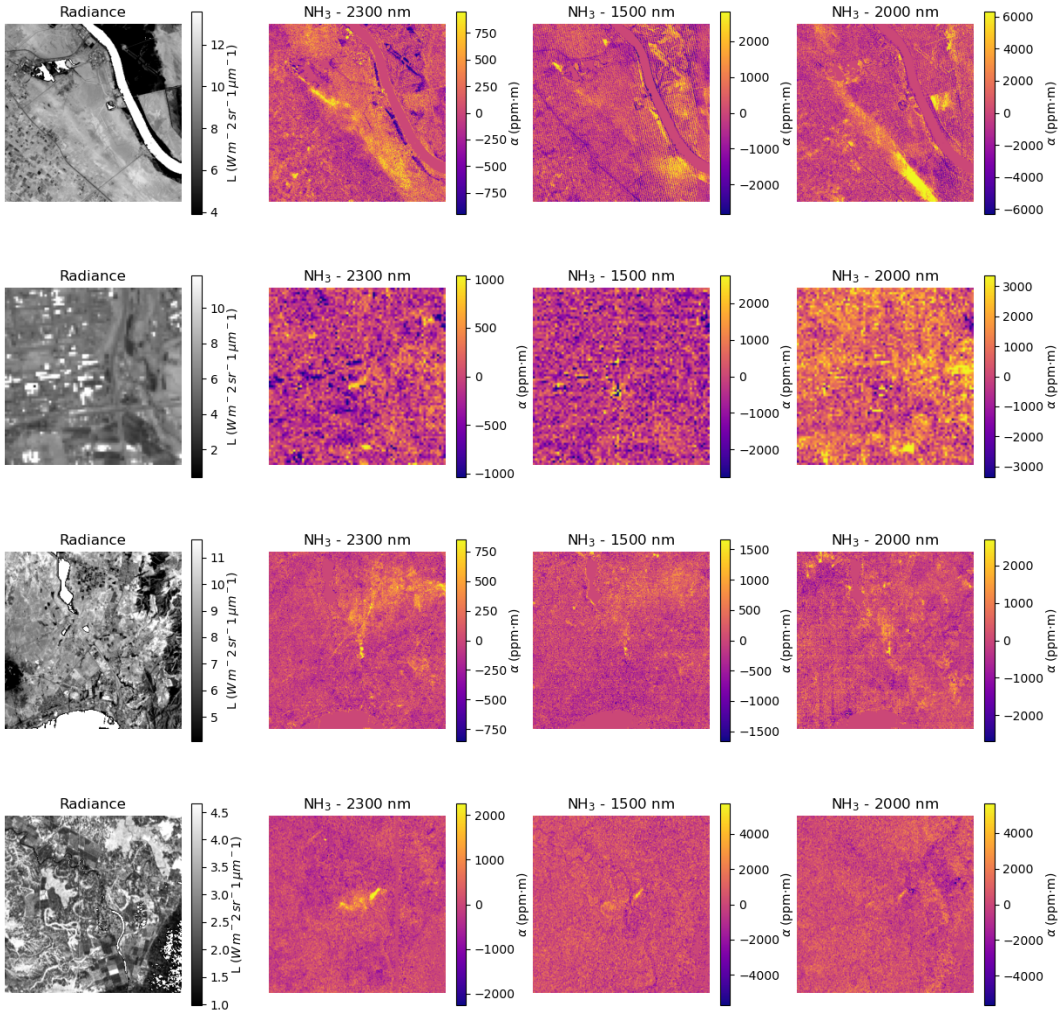

Figure S7: Analysis of plume detection on several retrieval windows. From top to bottom: PRISMA-Iraq (2024-09-07), EnMAP-Uzbekistan (2025-07-06), EMIT-Algeria (2024-08-04), and GF-5A AHSI-India (2026-02-15). Starting from the left: radiance reference band and retrievals from the 2300 nm, 1500 nm, and 2000 nm windows.

Table S3: List of Ueff calibration parameters for the EnMAP, GF-5A AHSI, PRISMA, and EMIT instruments, where $U_{\text{eff}} = a \cdot U_{10} + b$.

Mission (τ)	**a**	**b**
EnMAP (∞)	0.42	0.68
EnMAP (1 h)	0.41	0.85
GF-5A AHSI (∞)	0.42	0.68
GF-5A AHSI (1 h)	0.41	0.85
PRISMA (∞)	0.43	0.61
PRISMA (1 h)	0.42	0.76
EMIT (∞)	0.47	0.70
EMIT (1 h)	0.45	0.90

the 2000 nm retrieval.

S5 Analyzing the correlation with other gases

In Figure S8, we show the unmasked retrievals of the emissions shown in Figure 3 together with retrievals of other gases for the EnMAP–Uzbekistan, GF-5A AHSI–India, EMIT–Algeria, PRISMA–Iraq, and MethaneSAT–Pakistan cases. Except for the latter, we show—starting from the left—the radiance band and the NH_3, CH_4, CO_2, and H_2O retrievals. For the MethaneSAT case, we only show the radiance band and the NH_3 and CH_4 retrievals. We could only observe a faint correlation among gases in the GF-5A AHSI case in the CH_4 retrieval, which is probably due to the overlapping absorption features between both gases together with the surface heterogeneity beneath the plume. In this situation, the matched filter may struggle to clearly distinguish between both gases.

S6 Selection of the best retrieval for plume detection

Previously in the text, we mentioned that the use of a wider spectral range as in Roger et al. (2024b) was not considered in the sensitivity analysis due to the large underestimation of plume pixel values. However, we test in a couple of examples whether it has some advantages compared to the 2300 nm window, which has been considered so far as the best option for plume detection. In Figure S9, we show two scenes acquired by the GF-5A AHSI (top) and EnMAP (bottom) missions in India and Pakistan, respectively. We show a reference radiance band (left panel), the retrieval based on the 2300 nm window (center panel), and the one based on the wide-window matched filter (WWMF) (right panel), which we applied in the 1400–2500 nm range. The plume source is pinpointed with a red dot. Also note that the

retrieval color bar upper limit was defined as two standard deviations of the retrieval values, allowing the color scale to reflect the variability of each retrieval rather than using a common upper limit that could be misleading. For the GF-5A AHSI case, even though we observe in the WWMF that there are areas where random noise is more pronounced, we also see other areas with reduced noise and generally a clear attenuation of retrieval artifacts. For the EnMAP case, a slight increase in random noise in the WWMF is found together with the appearance of new artifacts. However, a strong artifact next to the source that could be misinterpreted as part of the plume is considerably attenuated.

As observed, extending the retrieval window also implies the risk of including new artifacts due to confounders in other parts of the spectrum and higher random noise, since we include gas absorption features that are more challenging to distinguish from background. In order to solve this issue for methane, Roger et al. (2024b) accepted as plume pixel candidates only those obtained from the main retrieval window. Those plume pixel candidates arising from the WWMF that did not appear in the main retrieval were penalized. In this manner, the appearance of new clutter and artifacts was attenuated. Similar operations might also be applied to ammonia retrieval.

S7 Time-series assessment of a fertilizer plant in Iraq

As in Guanter et al. (2025), we use multivariate Monte Carlo simulations and polynomial fits to derive the mean emission rate curve over time together with the corresponding uncertainty. For the Monte Carlo samples, we assumed a 50% correlation among flux rate errors and we set the uncertainty to two standard deviations of the multivariate distribution to account for the large scatter and scarcity of points. Regarding the polynomial fit, we tested polynomials from first to fourth order (see Figure S10). Third- and fourth-order polynomials showed variations in the trend that were clearly due to overfitting the scatter. Among the first- and second-order polynomials, we selected the latter because it better captures realistic long-term variations instead of a purely linear trend. However, we acknowledge that even assuming two standard deviations for the time series uncertainty we find a mismatch with the instrument measurements. A larger number of points would be needed to create a more robust estimation.

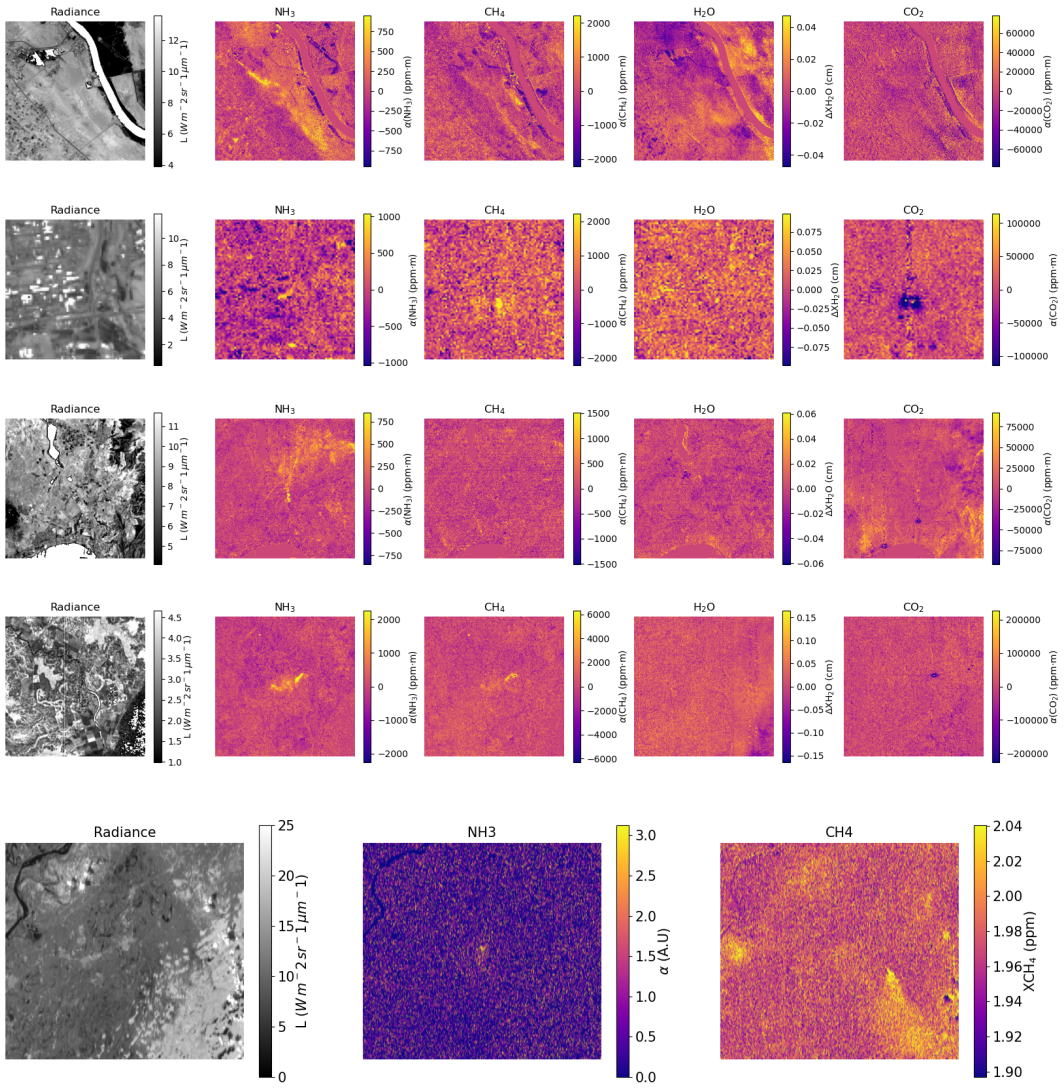

Figure S8: Analysis of potential emission correlation with other gas retrievals. From top to bottom: PRISMA-Iraq (2024-09-07), EnMAP-Uzbekistan (2025-07-06), EMIT-Algeria (2024-08-04), GF-5A AHSI-India (2026-02-15), MethaneSAT-Pakistan (2024-09-11). Starting from the left: radiance reference band, ammonia (2300 nm window), CH_4, H_2O, and CO_2 retrievals. In the case of Methanesat: radiance reference band, ammonia (1650 nm window), and CH_4 retrievals.

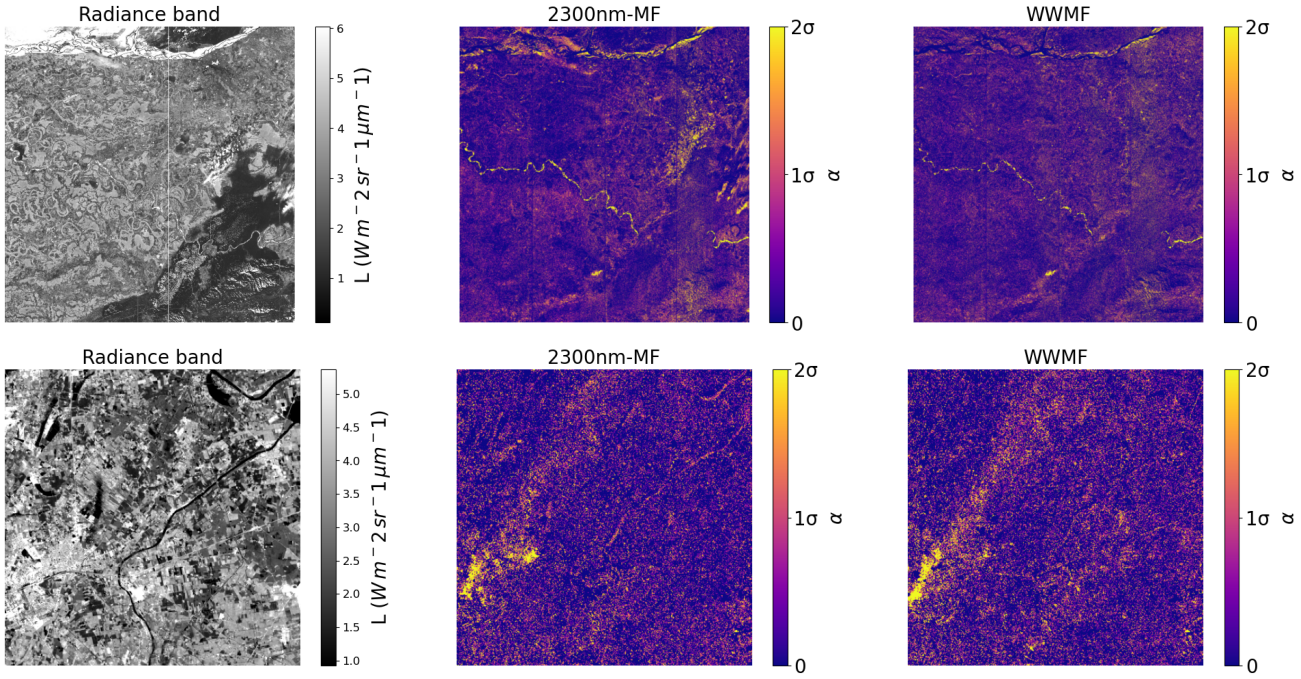

Figure S9: Assessment of the WWMF retrieval performance. GF-5A AHSI-India (2026-02-15) (top) and EnMAP-Pakistan (2024-11-20) (bottom). Sources are indicated with a red point. Starting from the left: radiance reference band, ammonia (2300 nm window), and ammonia (WWMF) retrievals.

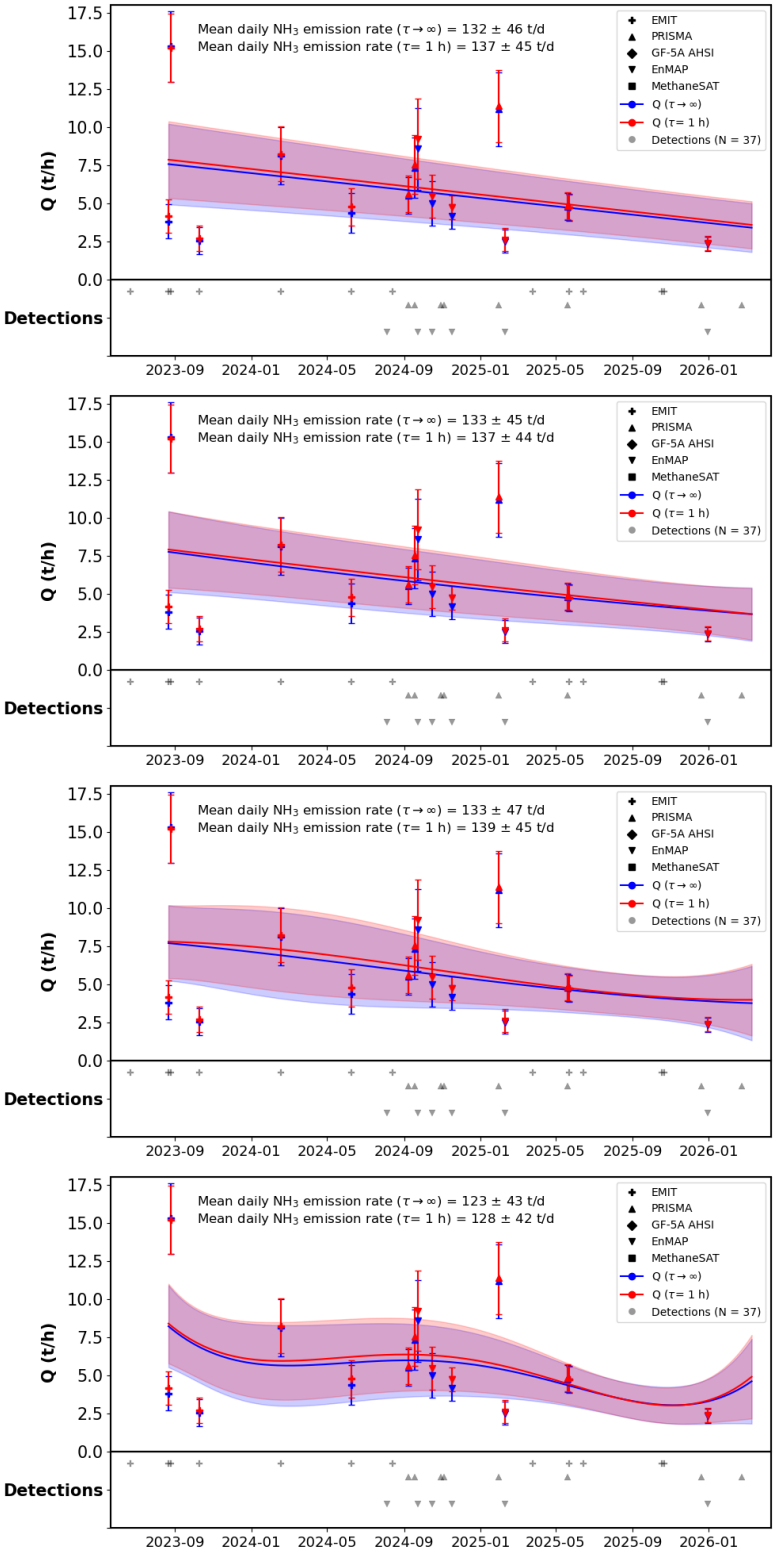

Figure S10: Time series of ammonia emissions from a fertilizer plant in Iraq during the period from September 2023 to March 2026. Detections are shown in gray, while quantified emissions are shown in blue and red when considering $\tau \to \infty$ and $\tau = 1$ h, respectively. From top to bottom, 1st-, 2nd-, 3rd-, and 4th-order polynomial fits together with their uncertainties for both τ values are shown. Mean daily ammonia emission rate values are displayed at the top of each panel.

References

1. Dudhia, A. The reference forward model (rfm). *Journal of Quantitative Spectroscopy and Radiative Transfer* **186**, 243–253 (2017). URL https://www.sciencedirect.com/science/article/pii/S0022407316301029. Satellite Remote Sensing and Spectroscopy: Joint ACE-Odin Meeting, October 2015.

2. Bertin, T. *et al.* The hitran2024 methane update. *Journal of Quantitative Spectroscopy and Radiative Transfer* **349**, 109736 (2026). URL https://www.sciencedirect.com/science/article/pii/S002240732500398X.

3. Eriksson, P., Buehler, S., Davis, C., Emde, C. & Lemke, O. Arts, the atmospheric radiative transfer simulator, version 2. *Journal of Quantitative Spectroscopy and Radiative Transfer* **112**, 1551–1558 (2011). URL https://www.sciencedirect.com/science/article/pii/S0022407311001105.

4. Mlawer, E., Cady-Pereira, K., Mascio, J. & Gordon, I. The inclusion of the MT_CKD water vapor continuum model in the hitran molecular spectroscopic database. *Journal of Quantitative Spectroscopy and Radiative Transfer* **306**, 108645 (2023). URL https://www.sciencedirect.com/science/article/pii/S0022407323001632.

5. Mayer, B. & Kylling, A. Technical note: The libradtran software package for radiative transfer calculations - description and examples of use. *Atmospheric Chemistry and Physics* **5**, 1855–1877 (2005). URL https://acp.copernicus.org/articles/5/1855/2005/.

6. Foote, M. D. *et al.* Impact of scene-specific enhancement spectra on matched filter greenhouse gas retrievals from imaging spectroscopy. *Remote Sensing of Environment* **264**, 112574 (2021). URL https://www.sciencedirect.com/science/article/pii/S0034425721002947.

7. Carmona, E. Personal communication. Email (2024). Communicated on February 15, 2024.

8. Thompson, D. R. Personal communication. Email (2024). Communicated on March 6, 2024.

9. Roger, J., Guanter, L., Gorroño, J. & Irakulis-Loitxate, I. Exploiting the entire near-infrared spectral range to improve the detection of methane plumes with high-resolution imaging spectrometers. *Atmospheric Measurement Techniques* **17**, 1333–1346 (2024). URL https://amt.copernicus.org/articles/17/1333/2024/.

10. Madhavan, S. & Sathe, S. Y. Inspection of ammonia plants. *Plant/Operations Progress* **6**, 35–41 (1987). URL https://aiche.onlinelibrary.wiley.com/doi/abs/10.1002/prsb.720060110. https://aiche.onlinelibrary.wiley.com/doi/pdf/10.1002/prsb.720060110.

11. Agency for Toxic Substances and Disease Registry (ATSDR). Toxicological profile for ammonia. Toxicological Profile TP-126, U.S. Department of Health and Human Services, Public Health Service, Atlanta, GA (2004). URL https://www.atsdr.cdc.gov/toxprofiles/tp126-c2.pdf.

12. Gorroño, J., Pei, Z. & Guanter, L. Benchmark simulations for methane emissions validation and sensitivity studies (2026). URL https://doi.org/10.5281/zenodo.18161182.

13. Gorroño, J., Pei, Z., Valverde, A. & Guanter, L. Considering the observation and illumination angular configuration for an improved detection and quantification of methane emissions. *Atmospheric Measurement Techniques* **19**, 1245–1257 (2026). URL https://amt.copernicus.org/articles/19/1245/2026/.

14. Van Damme, M. *et al.* Industrial and agricultural ammonia point sources exposed. *Nature* **564**, 99–103 (2018). URL https://doi.org/10.1038/s41586-018-0747-1.